NUMERICAL SIMULATION OF THERMAL-HYDROLOGICAL AND THERMAL-MECHANICAL PROCESSES OBSERVED AT THE DRIFT-SCALE HEATER TEST AT YUCCA MOUNTAIN, NEVADA

R.T. Green[1], S.M. Hsiung[1], S.L. Painter[1], A.H. Chowdhury[1], and M.S. Nataraja[2]
[1]Center for Nuclear Waste Regulatory Analyses, U.S.A.
[2]U.S. Nuclear Regulatory Commission, U.S.A.

Abstract: Results from the 4 year-long heating phase of the Drift-Scale Heater Test at the Exploratory Studies Facility at Yucca Mountain, Nevada, provide a basis to evaluate conceptual and numerical models used to simulate thermal-hydrological and thermal-mechanical coupled processes expected to occur at the potential geologic repository at Yucca Mountain. The objectives of the evaluation were to investigate coupled processes associated with (i) temperature effects on mechanical deformation (ii) temperature effects on moisture redistribution, (iii) temperature evolution through rock mass of variable saturation, and (iv) effect of thermal-mechanical processes on rock-mass permeability. Two- and three-dimensional numerical models were built to perform the thermal-mechanical and thermal-hydrological analyses. Thermal-hydrological model simulations were predicated on a dual (fracture and matrix) continuum conceptualization, while the thermal-mechanical simulations were predicated on a continuum representation of a deformation-permeability relationship based on fracture normal stress. A 30-percent reduction in the canister heat load to account for conduction and radiation heat loss through the bulkhead, a constant pressure boundary condition at the drift wall, and inclusion of the active fracture model to account for a reduction in the number of fractures that were hydraulically active provided the best agreement between model results and observed temperatures in the coupled thermal-hydrological analyses. The estimated trend of permeability responses using a normal stress-based deformation-permeability relationship compared reasonably to that measured in the coupled thermal-mechanical analyses.

1. INTRODUCTION

The Drift-Scale Heater Test at the Exploratory Studies Facility at Yucca Mountain, Nevada, is a planned 8 year-long *in-situ* heater test, with 4 years of heating followed by 4 years of cooling. The test has been monitored using a vast array of instrumentation to measure, or infer, changes in temperature, saturation, displacement, and chemistry. The 4-year heating phase was initiated in December 1998 and completed in January 2002. Results from the Drift-Scale Heater Test contribute to the basis for evaluating the capability of coupled-processes codes to simulate thermal-mechanical-hydrological-chemical processes in partially saturated fractured rock. Thermal-hydrological and thermal-mechanical coupled processes are analyzed in this paper.

For the modeling study presented here, temperature, saturation, and mechanical deformation distributions in the rock were simulated for the 4-year heating phase of the Drift-Scale Heater Test. Model results were compared with measured temperatures, saturations, and fracture permeability at the onset of the test and with measured temperatures and fracture permeability changes after 3 months, 1 year, and 4 years of heating. This paper presents the modeling results of (i) temperature effects on mechanical deformation (ii) temperature effects on moisture redistribution, (iii) temperature evolution through rock mass of variable saturation, and (iv) effect of thermal-mechanical processes on rock-mass permeability and their comparison with the measured data. These modeling studies are an important part of the process of assessing and developing confidence to independently evaluate the safety case for the potential geologic repository at Yucca Mountain. The modeling analyses reported in this paper were conducted as part of coupled-processes comparative studies of the DECOVALEX III program.

2. DRIFT-SCALE HEATER TEST DESCRIPTION

The Drift-Scale Heater Test is located in the Topopah Spring middle nonlithophysal (Tptpmn) unit, within the horizon of the potential repository at Yucca Mountain. The Tptpmn unit is approximately 30–40 m thick at the location of the Drift-Scale Heater Test, overlain by the Topopah Spring upper lithophysal (Tptpul) unit and underlain by the Topopah Spring lower lithophysal (Tptpll) units. The Drift-Scale Heater Test block was characterized prior to the onset of heating. Onsite characterization of the local geology and *in-situ* hydrology was supplemented with laboratory tests of thermal-hydrological and thermal-mechanical properties.

A plan-view schematic of the relative placement of the heated drift to the observation drift is shown in Figure 1. The 5-m-diameter, 47.5-m-long heated drift is closed at the east end by a thermal bulkhead. Approximately 12 m of the west end of the heated drift is lined with cast-in-place concrete ground support. Mesh and rock bolts provide support for the remainder of the drift. Concrete inverts were placed along the entire floor of the heated drift to provide a flat surface. Thermal sources consist of 9 canister heaters, placed end to end on the floor of the heated drift, and 50 wing heaters (25 on either side), emplaced in horizontal boreholes drilled perpendicular into the sidewalls of the heated drift about 0.25 m below the springline. The wing heaters are spaced 1.83 m apart. Each wing heater has two segments, both 5 m long, separated by 1.67 m with a larger power output to the outer segment. The inner wing heater segment is separated from the heated drift wall by 1.5 m.

3. CONCEPTUAL MODELS

Separate conceptual and numerical models were used to simulate thermal-mechanical and thermal-hydrological coupled processes in the fractured rock at the Drift-Scale Heater Test. The approach used to simulate thermal-mechanical coupled processes was to first determine the effects of temperature on deformation of the rock, then to determine the change in permeability in response to deformation. In deformable rocks, changes in matrix permeabilities are likely to be small, consequently contributions of the rock matrix deformation-induced permeability change to the overall permeability are likely to be small. With this understanding, only the effects of mechanically induced fracture deformation on the rock-mass permeability were considered and a single continuum model was used to represent fracture permeability. The thermal-mechanical analyses were conducted in two dimensions based on a single continuum model using the FLAC code (Itasca Consulting Group, Inc., 2000).

Thermal-hydrological analyses were performed with a three-dimensional numerical model using the multiphase simulator MULTIFLO (Painter, et al., 2001; Lichtner and Seth, 1996). A variably sized grid in the xz-plane, commonly referred to as an unstructured grid, was used to construct the numerical model. This allowed for higher resolution near the heated drift and the wing heaters, areas with the greatest gradients in temperature and saturation. The xz-plane was extruded as 14 planes in the y-direction to give the model its third dimension. The medium was represented as a dual continuum, one for the matrix and one for the fractures. The dual continuum conceptualization implemented the active fracture model by Liu, et al. (1998) and two other matrix-fracture interactive conceptual models provided in MULTIFLO. Following are descriptions of these thermal-mechanical and thermal-hydrological conceptualizations.

3.1 Single Continuum Thermal-Mechanical Model

FLAC uses a time-marching method to solve a set of algebraic equations of motion and constitutive relations. In a continuous solid body, the equation of motion can be generalized as follows

$$\rho \frac{\partial \dot{u}_i}{\partial t} = \frac{\partial \sigma_{ij}}{\partial x_j} + \rho g_i \qquad (1)$$

where ρ is the mass density, t is time, $\dot{u}_i$ are components of the velocity vector, x_j are components of the coordinate vector, σ_{ij} are components of the stress tensor, g_i are components of the gravitational acceleration, and indices i and j are components in a Cartesian coordinate system.

The strain rate associated with the equation of motion may be derived from the velocity gradient using the following

$$\dot{e}_{ij} = \frac{1}{2}\left[\frac{\partial \dot{u}_i}{\partial x_j} + \frac{\partial \dot{u}_j}{\partial x_i} \right] \qquad (2)$$

where $\dot{e}_{ij}$ are strain-rate components. With the strain-rate known, the constitutive relation that describes the stress-strain relationship of a deformable body for an isotropic elastic material can be represented by

$$\Delta \sigma_{ij} = \{\delta_{ij}\left[K - \frac{2}{3}G\right]\dot{e}_{kk} + 2G\dot{e}_{ij}\}\Delta t \qquad (3)$$

where δ_{ij} is the Krönecker delta, Δt is the timestep, and K and G are bulk and shear moduli.

In FLAC, the large-strain condition can be accounted for, if the option is selected, by adding the rotation-induced stress component expressed in the following term to the stress components in Eq. (3)

$$\omega_{ik}\sigma_{kj} - \sigma_{ik}\omega_{kj} \qquad (4)$$

where

$$\omega_{ij} = \frac{1}{2}\left[\frac{\partial \dot{u}_i}{\partial x_j} - \frac{\partial \dot{u}_j}{\partial x_i} \right]\Delta t \qquad (5)$$

Formulation of thermally induced stresses

Temporal and spatial domain temperature change data input was used to calculate thermally induced stress changes using the FLAC code. Changes in the state of stresses, as a result of temperature change, generate an out-of-balance force for the modeled system. The effect of temperature change on stress variation is defined as

$$\Delta\sigma_{ij} = -\delta_{ij}\, 3\, K \alpha \Delta T \quad (6)$$

where α is the thermal expansion coefficient, and ΔT is the temperature change. Equation (6) is for a plane strain condition.

Effect of fracture normal stress

The change in fracture aperture resulting from the change in fracture normal stress prior to tensile failure may be estimated by a fracture normal closure model proposed by Barton and Bandis (1982). This model describes the relationship of fracture normal stress, σ_n, and the associated fracture closure, u_n, using the following

$$\sigma_n = \frac{u_n}{a - c u_n} \quad (7)$$

where a and c are constants and the compressive σ_n is assumed to be positive in value. An example of the relationship between fracture normal stress and fracture closure is presented as the curve in Figure 2. This relationship indicates that a fracture is mostly compressed at small normal stress levels. The fracture becomes more difficult to compress as the normal stress increases. Eventually, a maximum fracture deformation level is achieved, beyond which the fracture can no longer be compressed. This maximum deformation level ($u_{n\,\max}$) is called maximum possible closure.

Fracture tensile normal stress (negative in value) is possible for those cases when fracture tensile strength exists. Equation (7) is not adequate to account for a possible tensile normal stress condition. To accommodate this, Eq. (7) is extended by including an appropriate fracture tensile strength. In this study, σ_n is defined to represent the term $\sigma_n + \sigma_t$ where σ_t is the fracture tensile strength or the assumed tensile strength of the rock mass. Fracture dilation due to tension occurs when σ_n is greater than the fracture tensile strength, σ_t. Equation (7) can be expressed as fracture closure, u_n, as follows

$$u_n = \frac{a\sigma_n}{c\sigma_n + 1} \quad (8)$$

Preferably, the constants a and c are empirically determined using laboratory tests or field measurements. In this study, numerical values of these two constants had to be estimated because neither laboratory tests nor field measurements were available. Bandis, et al. (1983) suggest the constant a in Eqs. (7) and (8) can be approximated from the initial stiffness, K_{ni}, of the fracture

$$a = \frac{1}{K_{ni}} \qquad (9)$$

and the maximum possible closure of the fracture, $u_{n\max}$, may be defined as

$$u_{n\max} = \frac{a}{c} \qquad (10)$$

Results from laboratory experiments indicated the compressibility of fracture decreased as applied normal stress increased. A fracture no longer can be compressed when a limiting aperture or the maximum possible closure is reached (Witherspoon, et al., 1980; Bandis, et al., 1983; Barton, et al., 1985; Schrauf and Evans, 1986; Hsiung, et al., 1994). This limiting aperture is believed to be fracture-roughness and fracture wall-strength dependent. The limiting aperture is called the residual fracture aperture, b_{res} (Figure 2). This residual fracture aperture is assumed to be small and can be neglected. With this assumption, $u_{n\max}$ can be related to the fracture aperture $b_{0,}$, which is related to those cases when fracture normal stress, σ_n (or $\bar{\sigma}_t$ for this study), is 0 (Figure 2).

$$b_0 = u_{n\max} = \frac{a}{c} \qquad (11)$$

With the relationship in Eq. (11) established, the reference fracture aperture, b_r, for the reference fracture permeability and porosity at the reference fracture normal stress, σ_{nr}, can be determined using the following equation

$$b_r = b_0 - u_{nr} \qquad (12)$$

where u_{nr} is the fracture closure at σ_{nr}. By incorporating Eqs. (8) and (11), Eq. (12) can be rewritten as

$$b_r = \frac{a}{c} - \frac{a\sigma_{nr}}{c\sigma_{nr} + 1} = \frac{a}{c(c\sigma_{nr} + 1)} \qquad (13)$$

Equation (13) may be manipulated to

$$\sigma_{nr}c^2 + c - \frac{a}{b_r} = 0 \qquad (14)$$

The quadratic equation is used to determine the constant c

$$c = \frac{-1 \pm \sqrt{1 + \dfrac{4\sigma_{nr} a}{b_r}}}{2\sigma_{nr}} \qquad (15)$$

Although c can be determined using Eq. (15), the reference fracture aperture, b_r, is still a difficult quantity to obtain. It is, therefore, necessary to replace the reference fracture aperture, b_r, with some known measurements. It should be noted that the fracture aperture, b, of a fracture set can be related to its corresponding fracture porosity, ϕ_f, and the fracture density, f_d, for any fracture normal stress, σ_n, using the following equation (cf. Snow, 1968)

$$b = \frac{\phi_f}{f_d} \qquad (16)$$

and the fracture-set permeability, k_f, for a set of fractures can be characterized by b and f_d using the following equation (Elsworth, 1989; Elsworth and Mase, 1993; Ofoegbu, 2000)

$$k_f = f_d \frac{b^3}{12} \qquad (17)$$

Replacing f_d in Eq. (16) with that in Eq. (17), b can be expressed in terms of k_f and ϕ_f

$$b = \sqrt{\frac{12 k_f}{\phi_f}} \qquad (18)$$

For a predetermined reference fracture normal stress level, the corresponding reference fracture aperture, b_r, then becomes

$$b_r = \sqrt{\frac{12 k_{fr}}{\phi_{fr}}} \qquad (19)$$

where k_{fr} and ϕ_{fr} are the reference fracture permeability and porosity of a fracture set. Replacing b_r in Eq. (15) with that in Eq. (19), c can now be estimated with known variables

$$c = \frac{-1 \pm \sqrt{1 + 4\sigma_{nr} a \sqrt{\dfrac{\phi_{fr}}{12 k_{fr}}}}}{2\sigma_{nr}} \qquad (20)$$

With constants *a* and *c* known, fracture aperture, *b*, can be determined for any given fracture normal stress level.

Fracture dilation of fractured rocks

The change in fracture permeability caused by plastic deformation of a fracture set may be estimated by assuming that the change in fracture porosity, $\Delta\phi_{fp}$, can be defined

$$\Delta\phi_{fp} = e_{ftp} + e_{fsp} \tan\psi_f \qquad (21)$$

where e_{ftp} is the plastic strain caused by tensile failure of the fracture set, e_{fsp} is the plastic shear strain of the fracture set, and ψ_f is the dilation angle of the fracture set.

In this study, both the Mohr-Coulomb failure criterion and the ubiquitous fracture failure criterion were used to evaluate the mechanical effect on rock-mass permeability. For cases using the Mohr-Coulomb failure criterion, e_{ftp}, e_{fsp}, and ψ_f were assigned values representing the rock mass, while for cases using the ubiquitous fracture failure criterion, e_{ftp}, e_{fsp}, and ψ_f were assigned values representative of the fracture set.

Continuum representation for mechanical effect on fractured rock permeability

Knowing the fracture normal stress, σ_n, and fracture plastic strains, e_{ftp} and e_{fsp}, the effective fracture aperture at that fracture normal stress level is the sum of the reversible aperture as a function of fracture normal stress and the fracture plastic deformation. The effective fracture aperture can be determined by

$$b = b_0 - u_n + \Delta b_p \qquad (22)$$

where Δb_p is the aperture change caused by fracture plastic deformation such that

$$\Delta b_p = \frac{\Delta\phi_{fp}}{f_d} \qquad (23)$$

Variables in the right-hand side of Eq. (22) can be replaced by Eqs. (8), (11), and (23) to obtain

$$b = \frac{a}{c} - \frac{a\sigma_n}{c\sigma_n + 1} + \frac{\Delta\phi_{fp}}{f_d} = \frac{a}{c(c\sigma_n + 1)} + \frac{\Delta\phi_{fp}}{f_d} \qquad (24)$$

Using Eq. (20), Eq. (24) can be rewritten as

$$b = \frac{a}{c(c\sigma_n + 1)} + \frac{e_{ftp} + e_{fsp} \tan \psi_f}{f_d} \qquad (25)$$

By normalizing Eq. (17) with the reference fracture permeability, k_{fr}, and applying Eq. (25), a general mathematical form representing the mechanical effect on fracture permeability can be obtained

$$\frac{k_f}{k_{fr}} = \frac{f_d \frac{b^3}{12}}{f_d \frac{b_r^3}{12}} = \left[\frac{a}{c(c\sigma_n + 1)} \frac{1}{b_r} + \frac{e_{ftp} + e_{fsp} \tan \psi_f}{f_d b_r} \right]^3 \qquad (26)$$

Notice that $f_d\ b_r$ is equal to ϕ_{fr} [Eq. (16)] and that b_r can be expressed as shown in Eq. (19); consequently, Eq. (26) can be rewritten as

$$k_f = k_{fr} \left[\frac{a}{c(c\sigma_n + 1)} \sqrt{\frac{\phi_{fr}}{12 k_{fr}}} + \frac{e_{ftp} + e_{fsp} \tan \psi_f}{\phi_{fr}} \right]^3 \qquad (27)$$

3.2 Dual Continuum Thermal-Hydrological Model

Formulation of a dual continuum model

The fractured porous rock at the Drift-Scale Heater Test was represented in the coupled thermal-hydrological analyses using a dual continuum model. The DCM formulation is comparable to the dual permeability model (DKM) formulation (TRW Environmental Safety Systems, Inc., 2000). The DCM and DKM conceptualizations provide separate continua for the matrix and the fractures. The dual continuum are coupled throughout the model domain by transfer functions for heat and mass transfer between the fractures and matrix. Use of a DCM increases the complexity of the numerical model used in the simulations, but offers the potential to realistically partition flow between matrix and fractures. Formulation of the dual continuum is presented in context of MULTIFLO, the code used to implement this conceptualization. Of primary concern is how interaction between the two continua is implemented. There are three options for modifying the matrix-fracture interaction: (i) Option 1: constant relative permeability reduction; (ii) Option 2: factor reducing interfacial area; and (iii) Option 3: active fracture model (Liu, et al., 1998). The formulation for each option is described in the discussion.

In the MULTIFLO implementation of the dual continuum model, the relative permeability functions for flow from matrix to the fractures may be specified independently from the relative permeability for the fracture continuum. When $P_{lm} > P_{lf,}$ liquid flow is from the matrix to the fracture continuum and is modeled as

$$q_l = \frac{k_{\text{harmonic}} k_{rl,m\rightarrow f}}{\mu_l} \frac{P_{lm} - P_{lf}}{d} \qquad (28)$$

where q is flux, P is pressure, μ is viscosity, and the m, f, l, and r subscripts denote matrix, fracture, liquid, and relative. Liquid-phase relative permeability, k_{rl}, is taken to be the upstream value in this case. For $P_{lm} > P_{lf}$, the upstream value is for the matrix. Fracture permeability is expressed as intrinsic. Liquid permeability, k_{harmonic}, is expressed as the harmonic mean.

For $P_{lf} > P_{lm,}$ liquid flow is from the fracture to the matrix and is defined by

$$q_l = \frac{k_{\text{harmonic}} k_{rl,f\rightarrow m}}{\mu_l} \frac{P_{lf} - P_{lm}}{d} \qquad (29)$$

where $k_{rl,f\rightarrow m}$ is the relative permeability for fracture-to-matrix flow.

An analogous form of Eqs. (30) or (31) defines mass flow of gas between the matrix and fracture continua

$$q_g = \frac{k_{\text{harmonic}} k_{rg}}{\mu_g} \frac{P_{gf} - P_{gm}}{d} \qquad (30)$$

where the g subscript denotes gas. Note that for gas flow between the matrix and fracture continua, the upstream relative permeability is always used.

Analogous to mass flow are expressions and relationships for heat flow. Heat flow across the matrix fracture interface is defined

$$q_{\text{heat}} = k_{\text{harmonic}} \frac{T_f - T_m}{d} \qquad (31)$$

Note that heat transfer and mass transfer across the matrix-fracture interface are coupled processes, but each responds to its respective driving forces calculated for the same distance, d. Gradients that drive mass and heat transfer are decreased when the block dimensions are increased (i.e., the differences in pressure or temperature between the two continua remain the same for each model element while the distance in which the difference occurs increases with an increased block size, thereby reducing the gradients).

Relative permeability functions

Spatially variable values for absolute rock permeability (variable in three spatial directions) and media characteristic curves for relative permeability and capillary pressure can be specified in MULTIFLO. Capillary saturation relations provided in MULTIFLO are based on either van Genuchten (1980),

linear, or Brooks-Corey (Brooks and Corey, 1966) functions. The van Genuchten relationship is used here.

Liquid-phase relative permeability, k_{rl}, is calculated using the Mualem relationship (Mualem, 1976)

$$k_{rl} = \sqrt{s_l^{\text{eff}}} \left\{ 1 - \left[1 - \left(s_l^{\text{eff}} \right)^{1/\lambda} \right]^{\lambda} \right\}^2 \qquad (32)$$

Saturation is related to the capillary pressure, P_c, by the van Genuchten relationship (van Genuchten, 1980)

$$s_l^{\text{eff}} = \left[1 + \left(\alpha |P_c| \right)^m \right]^{-\lambda} \qquad (33)$$

where effective liquid saturation, s_l^{eff}, is defined by

$$s_l^{\text{eff}} = \frac{s_l - s_l^r}{s_l^o - s_l^r} \qquad (34)$$

and where r and o denote residual and maximum saturations. The symbols α and λ are the van Genuchten parameters. λ is related to m in Eq. (35) by $\lambda = 1 - \gamma/m$.

The gas-phase relative permeability, k_{rg}, is defined as the complement of k_{rl}

$$k_{rg} = 1 - k_{rl} \qquad (35)$$

Option 1 in MULTIFLO allows the user directly to reduce the fracture-to-matrix relative permeability function by a constant factor. This reduction is incorporated by multiplying the relative permeability function by a relative permeability reduction factor, η,

$$k_{rl,f \to m} = \eta k_{rl,f} \qquad (36)$$

This application attenuates liquid flow from the fracture continuum to the matrix continuum, but allows heat and gas to flow unimpeded.

In Option 2, upstream values are used for the fracture-to-matrix relative permeability. In addition, the user can reduce the interfacial area between the matrix and fracture continua using the modifier A_{mod}, a term included to allow a reduction, but not an increase, in the interfacial area between the matrix and fracture continua. When liquid pressure in the matrix exceeds the pressures in the fractures (i.e., $P_{lm} > P_{lf}$), liquid flow, Q_l, from the matrix to the fracture continuum is defined by a modification of Eq. (28)

$$q_l = \frac{A_{\mathrm{mod}}}{\mu_f} k_{harmonic} k_{rl,m} \frac{P_{lm} - P_{lf}}{d} \qquad (37)$$

For $P_{lf} > P_{lm}$, flow from the fractures to the matrix is defined by a modification of Eq. (29)

$$q_l = \frac{A_{\mathrm{mod}}}{\mu_f} k_{harmonic} k_{rl,f} \frac{P_{lf} - P_{lm}}{d} \qquad (38)$$

Similarly, an analogous form of Equation 31 defines mass flow of gas, Q_g, between matrix and fracture continua.

$$q_g = \frac{A_{\mathrm{mod}}}{\mu_g} k_{harmonic} k_{rg} \frac{P_{gf} - P_{gm}}{d} \qquad (39)$$

In Option 3, a separate representation $k_{rl,f\to m}$ is used for flow from fracture to matrix, thereby providing additional flexibility.

The active fracture model for unsaturated flow through fractured rocks proposed by Liu, et al. (1998) was used to modify flow through fractures in Option 3. This model is based on the hypothesis that only a portion of connected fractures is active in conducting water. The hypothesis stipulates that (i) all connected fractures are active if the system is fully saturated, (ii) all fractures are inactive if the system is at residual saturation, and (iii) the fraction of fractures that is active is related to water flux through the fractures. Liu, et al. (1998) proposed that the fraction of active fractures be a power function of effective water saturation in connected fractures.

In the active fracture model, the liquid-phase relative permeability function for the fracture continuum defined in the Mualem relationship is modified to

$$k_{rl} = \left(S_l^{eff}\right)^{\frac{1+\gamma}{2}} \left\{1 - \left[1 - \left(S_l^{eff}\right)^{\frac{1-\gamma}{\lambda}}\right]^{\lambda}\right\}^2 \qquad (40)$$

to describe fracture to matrix flow. S^{eff} is effective saturation. Similarly, the van Genuchten relationship between effective saturation and capillary pressure is modified to

$$S_l^{eff} = \left[1 + \left(\alpha \left|P_c\right|\right)^{\frac{m}{1-\gamma}}\right]^{-\lambda} \qquad (41)$$

where α is the inverse of the air-entry pressure, P_c is capillary pressure, n and m are fitting parameters, and γ is a positive constant depending on the properties of the fracture network.

Relative permeability for fracture-to-matrix flow is specified as (Liu, et al., 1998)

$$k_{rl,f\to m} = \left(s_l^{\text{eff}}\right)^{\frac{3}{2}(1+\gamma)} \left\{ 1 - \left[1 - \left(s_l^{\text{eff}}\right)^{\frac{1-\gamma}{\lambda}} \right]^{\lambda} \right\}^2 \qquad (42)$$

The gas-phase relative permeability function is defined as the complement to the liquid-phase relative permeability,

$$k_{rg} = 1 - k_{rl} \qquad (43)$$

In summary, the three options for modifying the matrix-fracture interaction are:

- Option 1: Constant relative permeability reduction factor. In this option, $A_{\text{mod}} = 1$ and $k_{rl,f\to m} = \eta k_{rl,f}$ where $\eta < 1$. This option reduces liquid flow from matrix to fractures, but leaves all other fluxes unmodified.

- Option 2: Reducing interfacial area. In this option, A_{mod} is specified <1. The reduction in interfacial areas applies to all flows in both directions (fracture-to-matrix and matrix-to-fractures). The relative permeability for fracture to matrix flow is specified as the upstream (fracture) value $k_{rl,f\to m} = k_{rl,f}$.

- Option 3: Active fracture model. In this case, $A_{\text{mod}} = 1$, fracture-to-matrix relative permeability $k_{rl,f\to m}$ is specified by Eq. (42), fracture capillary pressures from Eq. (41), and fracture relative permeability from Eq. (40). All other fluxes are left unmodified.

4. NUMERICAL SOLUTION

4.1 Thermal-Mechanical Model

Thermal-mechanical numerical simulations of a two-dimensional vertical cross section of the Drift-Scale Heater Test were performed using FLAC (Itasca Consulting Group, Inc., 2000). The cross section is oriented perpendicular to the axis of the heated drift and is located 23 m from the thermal bulkhead. The FLAC model had dimensions of 1,000 m (width) and 740 m (height). A 5-m-diameter circular drift was located with its center 500 m from the left boundary and 500 m from the bottom of the model domain. The top boundary of the model coincided with the ground surface. The model included three thermal-mechanical lithologic units: Tptpul unit on the top, Tptpmn unit in the middle, and Tptpll unit on the bottom. The Tptpmn unit was 36 m thick, and its base was 482 m from the bottom of the model domain. The heated drift was located in the middle of the Tptpmn unit. A close-up view of the two-dimensional grid used in thermal-mechanical analyses is illustrated in Figure 3.

Rock-mass mechanical and strength properties are required by FLAC. Discontinuities in rock tend to soften and weaken the media, therefore, the deformation modulus of a rock mass could be substantially different from that of the intact rocks. Consequently, the rock-mass deformation modulus can exhibit large variations in the presence of joints. To consider discontinuities, CRWMS M&O (1999, 1997a) used the rock-mass quality category approach by dividing each rock unit into five rock-mass categories. The five rock-mass categories were defined based on cumulative frequency of occurrence of the discontinuities. The corresponding rock-mass properties were estimated using full peripheral-fracture mapping data. In this study, the corresponding rock-mass Young's moduli were used for modeling. Intact rock materials properties for the three rock units modeled are listed in Table 1 and Table 2 lists the rock-mass Young's modulus of each rock-mass category for Topopah Spring Welded Tuff Thermal-Mechanical Units 1 (TSW1) and 2 (TSW2). As can be observed in Table 2, rock-mass Young's modulus varies more than a factor of two from Rock-Mass Quality Category (RMQ) 1 to 5. Note that Tptpul is a part of TSW1, while Tptpmn and Tptpll are part of TSW2.

Table 1. Intact rock material properties (CRWMS M&O, 1997b and 1999)

Unit	**Tptpul**	**Tptpmn**	**Tptpll**
Bulk Density kg/m^3[lb/ft^3]	2,160 ± 80 [134.8 ± 5.0]	2,250 ± 70 [140.5 ± 4.4]	2,250 ± 60 [140.5 ± 3.7]
Young's Modulus, Gpa [10^6 psi]	20.36 ± 6.75 [2.95 ± 0.98]	33.03 ± 5.94 [4.79 ± 0.86]	33.03 ± 5.94 [4.79 ± 0.86]
Poisson's Ratio	0.23 ± 0.07	0.21 ± 0.04	0.21 ± 0.04

Table 2. Rock-mass Young's Modulus (CRWMS M&O, 1999)

	Rock-Mass Quality Category	**Cumulative Frequency of Occurrence**	**Rock-Mass Young's Modulus, GPa**
Thermal-Mechanical Unit	1	5%	9.03 [1.31]
	2	20%	14.28 [2.07]
Topopah Spring Welded Tuff Unit 1	3	40%	19.40 [2.81]
	4	70%	20.36 [2.95]
	5	90%	20.36 [2.95]
Topopah Spring Welded Tuff Unit 2	1	5%	8.98 [1.30]
	2	20%	12.02 [1.74]
	3	40%	14.77 [2.14]
	4	70%	18.92 [2.74]
	5	90%	24.71 [5.58]

FLAC accepts bulk and shear moduli (K and G) as material properties input using the following:

$$K = \frac{E}{2(1+\nu)} \qquad (44)$$

and

$$G = \frac{E}{3(1-2\nu)} \qquad (45)$$

where E and ν are Young's modulus and Poisson's ratio. Bulk properties are listed in Table 2.

Determining rock-mass strength properties is equally difficult, if not more, than determining the rock-mass deformation modulus. A rock-mass quality category approach was used to quantify rock-mass strength properties and associated uncertainties and variability (CRWMS M&O, 1999). Table 3 lists the intact rock strength properties and Table 4 lists the rock-mass strength properties for the two thermal-mechanical units mentioned previously. Note that, in this qualification system, rock mass with the higher RMQ number has relatively larger strength properties than rock mass with lower RMQ designations.

Table 3. Intact rock strength properties (CRWMS M&O, 1999)

Thermal-Mechanical Unit	**Cohesion, MPa [psi]**	**Tensile Strength, MPa [psi]**	**Friction Angle, Degree**	**Dilation Angle, Degree**
Topopah Spring Welded Tuff Unit 1	12.65 [1,834.3]	5.48 ± 2.32 [794.6 ± 336.4]	47.45	23.73
Topopah Spring Welded Tuff Unit 2	38.69 [5,610.1]	8.91 ± 3.39 [1.292 ± 491.6]	48.15	24.08

The strength properties for the Tptpul and the Tptpmn were assumed to be the same as the TSW1 and TSW2, respectively (CRWMS M&O, 1999). The Tptpll, however, might not be as strong as the Tptpmn unit even though these two units were grouped in the same thermal-mechanical unit (TSW2). The Tptpll contains voids of various sizes, compared with the Tptpmn that does not contain large voids. It is, therefore, reasonable to assume that the former unit is relatively weaker than the latter. Consequently, assigning the same strength properties to the Tptpll as the Tptpmn may not be appropriate. No strength data for the Tptpll are readily available; therefore, the strength properties for the TSW1 were assigned to the Tptpll.

However, the rock-mass friction angle for the Tptpmn unit was greater than the intact-rock friction angle. Therefore, for this unit, the intact-rock friction angle was used instead of the rock-mass friction angle. Two variations of rock-mass properties were modeled to study the sensitivity of rock-mass properties on the thermal-mechanical effects (Tables 3 and 4). Comparison of Tables 3 and 4 indicates that the rock-mass friction angles for the TSW2 appear to be larger than the intact-rock friction angle.

It is difficult to imagine that the rock-mass friction angle can be larger than the friction angle for intact rock. Sufficient information is not available to resolve this potential dilemma. For instances where the rock-mass friction angle was larger than the intact-rock friction angle, the intact-rock friction angle was used to represent the rock-mass friction angle. To be consistent, the rock-mass dilation angle was similarly adjusted.

Table 4. Rock-mass strength properties

Thermal-Mechanical Unit	Rock-Mass Quality Category (RMQ)	Cumulative Frequency of Occurrence	Cohesion, MPa [psi]	Tensile Strength, MPa [psi]	Friction Angle, Degree	Dilation Angle, Degree
Topopah Spring Welded Tuff Unit 1	1	5%	1.1 [159.5]	0.90 [130.5]	44	22
	2	20%	1.4 [203.0]	1.13 [163.9]	46	23
	3	40%	1.7 [246.5]	1.35 [195.8]	46	23
	4	70%	2.1 [304.5]	1.69 [245.1]	47	24
	5	90%	2.9 [420.5]	2.26 [327.7]	47	24
Topopah Spring Welded Tuff Unit 2	1	5%	1.9 [275.5]	1.16 [168.2]	56	28
	2	20%	2.3 [333.5]	1.36 [197.2]	57	29
	3	40%	2.6 [377.0]	1.54 [223.3]	57	29
	4	70%	3.2 [464.0]	1.82 [263.9]	58	29
	5	90%	3.9 [565.5]	2.22 [321.9]	58	29

The thermal expansion coefficients for the three litho-stratigraphic units were based on laboratory measurements (CRWMS M&O, 1997c)(Table 5). The temperature-dependent thermal expansion coefficient for each of the units varies more than a factor of 5 when temperature is increased from 25 °C to 300 ºC. The thermal expansion coefficients for both intact rock and rock mass were assumed the same. Thermal expansion coefficients corresponding to temperatures higher than 300 ºC were not available; therefore, values associated with 275–300 ºC were used for temperatures greater than 300 ºC.

Table 5. Thermal expansion coefficient data (10^{-6}/ºC) (CRWMS M&O, 1999)

Litho-Stratigraphic Unit	25–50 ºC	50–75 ºC	75–100 ºC	100–125 ºC	125–150 ºC	150–175 ºC
Tptpul	7.41	8.43	8.89	9.52	10.86	13.51
Tptpmn	6.89	8.45	8.95	9.50	10.12	10.95
Tptpll	6.41	8.15	8.77	9.12	9.87	10.75

Litho-Stratigraphic Unit	175–200 ºC	200–225 ºC	225–250 ºC	250–275 ºC	275–300 ºC
Tptpul	19.38	29.34	32.35	40.16	48.83
Tptpmn	12.09	14.57	19.45	27.24	41.56
Tptpll	12.55	15.14	25.19	26.15	33.40

Boundary and initial conditions

Initial *in-situ* stresses were consistent with overburden depth. Ambient temperatures (approximately 24 ºC) were applied to the boundaries of the model.

Model heat source

Thermal load was calculated based on the temperature distribution at the cross section 23 m from the thermal bulkhead. This cross section coincided with the location of vertical cross section in the numerical model. Thermal load is introduced into the thermal-mechanical model by specifying temperature at every model node as a function of time. Temperatures were measured during the Drift-Scale Heater Test at approximately 2,662 locations within the drift-scale heater test block. The temperature measurements in the rock were used to develop kriged temperature distributions at 1-m spacing and at 2-day intervals. Temperature data selected as input for analyses were at 3, 6, and 9 months, and 1, 2, 3, and 4 years of heating.

Figure 4 illustrates the contours of the temperature distribution of a vertical cross section located 23 m from the thermal bulkhead of the heated drift after 4 years of heating. The two high-temperature concentration zones located on either side of the heated drift coincide with the location of the wing heaters. The temperature field is asymmetrical even though the heaters were symmetrically placed with respect to the heated drift.

Rock failure criteria

The ubiquitous and Mohr-Coulomb fracture failure criterion were evaluated in this study. The fracture properties needed for the ubiquitous fracture failure criterion are listed in Table 6. The fracture tensile strength for all litho-stratigraphic units was assumed to be zero. Sensitivity of failure criteria to the

displacement and permeability for heated conditions was evaluated by replacing the ubiquitous fracture failure criterion with the Mohr-Coulomb failure criterion. Seven case studies were evaluated (Table 7). The failure criteria, rock-mass quality, and the thermal expansion coefficient were varied in the case studies. The ubiquitous failure criterion, RMQ 2 rock properties, and a temperature-dependent thermal expansion coefficient were assumed in the basecase (Case 4).

Table 6. Ubiquitous fracture failure criteria (CRWMS M&O, 2000)

Litho-Stratigraphic Unit	Fracture Orientation (counterclockwise from x axis), degree	Cohesion, MPa [psi]	Friction Angle, Degree	Dilation Angle, Degree
Tptpul	82.0	0.1 [14.5]	41	20.5
Tptpmn	83.5	0.1 [14.5]	41	20.5
Tptpll	80.5	0.1 [14.5]	41	20.5

Table 7. Case studies in the thermal-mechanical simulations. Case 4 was designated as the basecase.

Case No.	Rock-Mass Quality Category (RMQ)	Failure Criterion Used	Thermal Expansion Coefficient
1	2	Mohr-Coulomb	Temperature-Dependent
2	1	Mohr-Coulomb	Temperature-Dependent
3	5	Mohr-Coulomb	Temperature-Dependent
4 (basecase)	2	Ubiquitous	Temperature-Dependent
5	2	Mohr-Coulomb	Constant
6	1	Ubiquitous	Temperature-Dependent
7	2	Ubiquitous	Constant

4.2 Thermal-Hydrological Model

Thermal-hydrological analyses were performed with a three-dimensional numerical model using the multiphase simulator MULTIFLO (Painter, et al., 2001). A variably sized grid in the vertical plane, commonly referred to as an unstructured grid, was used to construct the numerical model. This allowed for higher resolution near the heated drift and the wing heaters, areas with the greatest gradients in temperature and saturation.

The numerical model grid was aligned with the axis of the heated drift. Vertical symmetry was assumed along and orthogonal to the drift axis. One plane of symmetry was placed mid-distance between the bulkhead and the terminus of the heated drift. The other plane was colinear with the drift axis. This allowed modeling only ¼ of the Drift-Scale Heater Test block volume. The vertical plane of the modeled area extended 200 m in the vertical direction and 100 m in the horizontal direction. The center of the heated drift was vertically placed at the midpoint of the model. The third dimension was modeled by extruding the H-direction of the drift as 14 planes. Planes that intersected the heated drift had 1,123 nodes for each continuum. Planes that did not intersect the heated drift had additional nodes to account for the drift (i.e., 1,175 nodes). The entire model, therefore, had 16,068 nodes in each continuum. Finer mesh resolution was included in areas expected to experience large-temperature, saturation, and pressure gradients (Figure 5).

Three hydrostratigraphic units are included in the model: Tptpul, Tptpmn, and Tptpll of the Topopah Spring welded unit. Values for key properties assigned to the three units are presented in Table 8 (CRWMS M&O, 2001). Property values are assigned uniformly to each unit. The medium was represented as a dual continuum, one for the matrix and one for the fractures. The basecase assumes these property values and the active fracture conceptual model.

Table 8. Key property values assigned to modeled units.

Unit	**Tptpul**	**Tptpmn**	**Tptpll**
Fracture permeability (m^2)	5.50e-13	2.76e-13	1.29e-12
Fracture porosity (–)	0.0066	0.010	0.011
Matrix Permeability (m^2)	3.08e-17	4.04e-18	3.04e-17
Matrix Porosity (–)	0.154	0.110	0.131
Thermal conductivity (dry)(W/m-K)	0.79	1.56	1.20
Thermal conductivity (wet)(W/m-K)	1.68	2.33	2.02
Bulk Density (kg/m^3)	2,160	2,250	2,250

Boundary and initial conditions

The vertical boundaries of the model were specified as adiabatic with no fluid flow. The top boundary was prescribed as a mixed boundary with specified flux and constant temperature and pressure. The bottom boundary was prescribed as a mixed type with specified pressure, temperature, and gravity drainage. The mixed boundary condition at the top allowed gas and heat transport in or out of the model while maintaining pressure and temperature as specified. The heated drift was not explicitly included in the model; instead, the heated drift wall was specified as constant pressure (at atmospheric), allowing for heat and mass loss out of the drift.

The temperature was specified as 22 and 26 ºC at the top and bottom model boundaries for a geothermal gradient of 0.02 ºC/m and a temperature of 24 ºC at the Drift-Scale Heater Test horizon. A static gas pressure difference of 2,156 Pa between the top and bottom boundaries was specified to impose a gas gradient consistent with ambient conditions. Initial saturation was determined by simulating flow in the absence of both heat and the presence of the drift at the Drift-Scale Heater Test for sufficiently long periods of time that steady-state flow conditions were approximated. An ambient

matrix saturation of 0.92 in the TSw34 (Tptpmn) was predicted at an infiltration rate of 0.06 mm/yr. An infiltration rate of 0.3 mm/yr corresponded with an ambient matrix saturation of 0.99.

Model heat source

Heat was applied in the Three-D thermal-hydrological model at the heated drift wall and at the locations of the inner and outer wing heaters. The heated drift cavity was not explicitly included in the model to avoid difficulties associated with representing the air space within the drift, radiative and convective heat transfer between the heater canisters and the drift wall, and the physics of heat and mass transfer at the drift-cavity/drift-wall boundary. The disadvantage to this simplification was that coupled thermal-hydrological processes at the drift wall could not be directly or easily investigated using this model.

The heat-source levels were applied uniformly to the drift boundary elements at the drift wall. The cylindrical wing heaters were represented as rectangular slabs, thereby smearing the heat deposition in the y-direction of the model. The Drift-Scale Heater Test experienced measured heat loads that deviated significantly (less) from the levels of the design heat loads since energized in December 1997. Piece-wise linear heat loads assigned to the model are compared with measured wing and canister heat loads in Figure 6. It was assumed that the decrease in cumulative heat load for the wing heaters occurred uniformly over both the inner and outer wing heaters. The canister heat load was reduced during the analyses to account for heat loss through the thermal bulkhead.

5. MODEL RESULTS

The thermal-mechanical model results were used to estimate thermally induced failure of rock mass, rock-mass deformation, and permeability changes. The thermal-hydrological model results were used to estimate evolution of temperature and saturation. Estimates from both were limited to the heating phase of the Drift-Scale Heater Test.

5.1 Thermally Induced Failure of Rock Mass

Thermal-mechanical modeling results indicated that, for all cases studied, the rock mass began to deform in response to the thermally induced stresses soon after the onset of heating. The selection of failure criterion had a distinct effect on the simulated thermally induced failure of rock mass. A comparison of rock yield typical for models with Mohr-Coulomb and ubiquitous fracture failure criteria is presented in Figure 7. As illustrated, rock yield for models with the ubiquitous fracture failure criterion typically occurred as fracture slip because of fracture shear failure. Conversely, yield zones developed in the Tptpul and Tptpll units at the interfaces with Tptpmn units for the models with the Mohr-Coulomb failure criterion.

Models with the Mohr-Coulomb fracture failure criterion simulated that the yield zone continued to grow upward throughout the heating process. The timing and ultimate size of the yield zone were rock-mass property dependent. This yield zone tended to develop earlier and greater for models with larger RMQ designations (e.g., RMQ 5 versus RMQ 2). This behavior is observed because the differences in Young's moduli among the RMQs are significant (i.e., thermally induced stresses are directly proportional to the Young's modulus), but the differences in the strength properties are relatively small.

Consequently, it is more likely for models with higher RMQ designations to develop yield zones larger than those with lower RMQ designations. A similar trend was observed in the development of a yield zone directly beneath the heated drift in the Tptpll at the interface with the Tptpmn. This yield zone, however, developed later and was smaller than the yield zone above the heated drift [Figure 7(a)].

Rock yielding in most models, which assumed the ubiquitous fracture failure criterion, occurred along fractures (fracture slip) because of fracture shear failure. As a result, the yielding behavior for the models using the ubiquitous failure criterion was substantially different from that for models using the Mohr-Coulomb failure criterion. The fracture slip zones were initiated in the Tptpmn unit during the early stage of heating, mainly in a diagonal direction, forming an approximately 45-degree angle counterclockwise from the vertical axis and more than 50 degrees from the fracture dip angles [Figure 7(b)]. Those fracture slip zones formed long shear bands stretching along the diagonal direction. As heating proceeded, new shear bands eventually formed larger vertical shear zones above and below the heated drift. Another group of shear bands developed later and expanded outward at an approximately 45-degree angle clockwise from the vertical axis through the heated drift. This shear zone developed at a much slower rate than the vertical shear zones. Similar to the yielding trend observed in the models with the Mohr-Coulomb failure criterion, the shear bands in models with ubiquitous failure criteria tended to develop earlier and more extensively in models with larger RMQ designations than in models with smaller RMQ designations.

5.2 Estimation of Rock-Mass Deformation

Rock-mass displacements were evaluated at the anchor locations of the four multiple-position extensometers (MPBXs) installed at the cross section of the drift approximately 21 m from the thermal bulkhead. For these four MPBXs, two were vertically oriented (one in the crown, MPBX9, and one in the invert, MPBX10) (Figure 8). The remaining two (MPBX7 and MPBX8) were inclined approximately 30 degrees from the vertical on either side of MPBX9. Each MPBX contained four anchors, with Anchor 1 the closest to the heated drift and Anchor 4 the farthest. Figures 9, 10, 11, and 12 show the measured and simulated displacements as a function of time for the basecase model (i.e., RMQ 2 rock-mass properties and the ubiquitous failure criterion). The letters E and M in the captions denote estimated results and measured data. The positive displacement shown in the figures indicates an anchor is moving away from the assembly head located at the drift wall of an MPBX.

In general, the model underestimated displacements, although simulated anchor displacements were larger when rock-mass properties with larger RMQ designations were used. During the early stage of heating, Anchor 4 for the two vertical MPBXs (i.e., MPBX9 and MPBX10) was simulated to move closer to the heated drift. Thereafter, Anchor 4 and the heated drift moved away from each other as heating proceeded. This phenomenon was not observed in the measured data. Instead, the measured data indicated that all anchors in each MPBX had almost identical displacements for the first few months of heating suggesting that only the rock mass between Anchor 1 and the assembly head deformed while there was negligible deformation in the rock mass between the other anchors.

After the early stage of heating, simulated anchor displacements relative to the MPBX assembly head were larger for the anchors located farther away from the heated drift, regardless of the rock-mass properties or failure criterion used. This displacement pattern indicated that the neighboring anchors of

an MPBX continued to move away from each other as heating proceeded, suggesting an expansion of the rock mass between all anchor pairs. This behavior was not strictly observed in the measured data where some compression zones could be identified in the rock mass between anchors; for example, between Anchors 1 and 3 of MPBX7 (Figure 9) and between Anchors 2 and 3 of MPBX9 (Figure 11) and MPBX10 (Figure 12).

One possible cause for the underestimation of displacement is attributed to the temperature data used in the modeling exercise. The temperature data set used in the displacement analyses was constructed by kriging the entire drift-scale heater test block in three directions at 1-m intervals. This kriging process had an advantage of providing temperature distributions for the entire block; however, the process inevitably introduced uncertainty by smoothing the measured temperature data. In particular, displacement could be underestimated near the heated drift if the temperature was reduced by kriging. Another possible cause might be that the seven thermal time intervals specified in the thermal-mechanical analysis were too coarse. Because plastic deformation is path dependent, it may be necessary to use smaller thermal timesteps to more realistically represent the plastic deformation behavior of the rock mass.

The measured displacements also suggested localized fracture slip. For example, fracture slip in the rock mass between Anchors 2 and 3 of MPBX7 after approximately 6 months of heating caused Anchor 3 to move relatively closer to the assembly head. Another example was the slip of a fracture, located possibly between Anchor 1 and the assembly head of MPBX7 at approximately 2.7–2.8 years of heating, that caused Anchor 1 to move closer to the assembly head. These slips caused a displacement reduction. A continuum analysis, such as that used in this study, could not capture this behavior. Consequently, displacements estimated by continuum modeling would not be able to predict displacement reduction representing fracture slip.

5.3 Thermal-Mechanical Effects on Rock-Mass Permeability

Permeability calculated using deformation estimates [Eqs. (20) and (27)] simulated by the continuum models was compared with permeability measured using pneumatic tests performed on hydrologic boreholes installed as part of the Drift-Scale Heater Test. Hydrologic boreholes were drilled and pressure sensors installed to measure permeability variations during the heating process. The simulated permeability variations at the pressure sensor locations in Boreholes 57 and 59 located at the cross section 10 m from the thermal bulkhead, and Boreholes 74 and 76, at the cross section 30 m from the thermal bulkhead (Figure 13), were compared with measured data. The reference values required by Eqs. (20) and (27) for normal stress and the fracture permeability and porosity are those measured prior to heating. The reference fracture permeability and porosity were 5.50×10^{-13} m^2 and 0.0066 for Tptpul, 2.76×10^{-13} m^2 and 0.01 for Tptpmn, and 1.29×10^{-12} m^2 and 0.011 for Tptpll (CRWMS M&O, 2001). The initial fracture stiffness was 2.01×10^5 MPa/m (CRWMS M&O, 1999).

Figures 14 and 15 illustrate that fracture permeability simulated for Boreholes 57 and 59 compared reasonably well with measured fracture permeability. Letters E and M in the legends denote estimated results and measured data. Vertical axes in the figures are the ratio of the current permeability to the reference permeability. In general, the trends of the simulated permeability in response to heating were

similar for all models regardless of the RMQ and failure criterion. Differences among the models were mainly confined to the magnitude of variation in the permeability.

One discrepancy between simulated and measured results was the variation in the permeability simulated at pressure sensor 1 (PS1) in Boreholes 57 and 59. Measurements at these locations indicated a reduction in permeability during the heating phase, whereas a permeability enhancement was simulated at the beginning of heating. The extent of the enhancement decreased as heating proceeded and, for some models analyzed, this enhancement disappeared and eventually led to a permeability reduction. The simulated reduction, however, was small in magnitude when compared with the measurements. Also, the measured data and modeling results of all models demonstrated different trends in permeability at PS1 in Borehole 59.

A recovery in permeability was observed at some pressure sensors during the middle of the heating phase following relatively large reductions of permeability experienced in the early heating phase. This recovery in permeability was not replicated in the simulations. Pressure sensors demonstrating this trend included PS2 and PS3 in Borehole 59 (Figure 15) and PS3 and PS4 in Borehole 76 (not shown). The permeability at PS3 in Borehole 59 not only completely recovered but also experienced a permeability enhancement between 3 and 4 years of heating. Two possible causes of the permeability recovery were identified. One possibility was a decrease in fracture normal stress that resulted in a reduction in fracture closure, which, in turn, increased the fracture aperture. When the fracture normal stress became smaller than the reference fracture normal stress, permeability enhancement would result. The other possibility was related to dilation induced by fracture shear displacement. This inability to predict permeability recovery limits the utility of the proposed deformation-permeability relationship; however, despite this limitation, the proposed deformation-permeability relationship provides an opportunity to investigate thermal-mechanical effects on rock-mass permeability using a continuum approach. Further studies are needed to explore this limitation to allow for calibration of this deformation-permeability relationship.

Simulated permeability variations within 60 m of the heated drift after 4 years of heating are illustrated in Figure 16 for the basecase model (i.e., RMQ 2 rock-mass properties and ubiquitous failure criterion). In general, a permeability reduction zone is simulated surrounding the heated drift. This effect was observed in models predicated on either failure criterion. The zone of reduced permeability extended diagonally outward from the upper-left and lower-right corners of the heated drift. The rock mass in the region immediately surrounding the heated drift exhibited the greatest reduction in permeability. Locations of high permeability were consistent with those of the shear bands shown in Figure 7(b). There also were isolated areas of permeability enhancement located in the permeability reduction zone. The same spatial permeability pattern was predicted regardless of which rock-mass properties were designated, if the same failure criterion was used, although the magnitude of change differed. In general, larger RMQ designation resulted in greater variations in permeability.

5.4 Thermal-Hydrological Coupled Processes

Coupled heat and mass transfer were simulated and compared to the Drift-Scale Heater Test data for the 4-year heating phase. Simulated temperatures were compared with measurements taken during the Drift-Scale Heater Test. Saturation for the rock matrix was inferred using geophysical methods (i.e., electrical resistivity tomography, ground-penetrating radar, and neutron logging). Saturation of the

rock fractures was inferred from air permeability test results. These measurements only provide a qualitative measure of saturation at the Drift-Scale Heater Test; therefore, only temperature measurements are compared with simulation results at this time, although inferred saturations may promote a clearer interpretation of the Drift-Scale Heater Test results.

The contour plots of simulated matrix saturation demonstrate distinguishable differences, particularly at 1 year of heating. One feature that differentiates the simulations was if the dryout zone associated with the boiling isotherm of the wing heaters and the heated drift completely coalesced by 1 year of heating. The dual continuum conceptualization with the area modifier A_{mod} reduced to 0.001 illustrates the simulation that has the least development of the dryout zone at 1 year (Figure 17a) when compared with the basecase (Figure 17b). Models with drift-wall heat reduced by 30 percent or with the van Genuchten α decreased by 10 times also demonstrated a decrease in the development of a dryout zone at 1 year of heating relative to the basecase simulation. Conversely, models with the matrix permeability increased by 10 times, thermal conductivity decreased by 20 percent, or with the van Genuchten α increased by 10 times exhibited the greatest development of a dryout zone at 1 year (e.g., see Figure 17c).

There were greater differences in simulated fracture saturations than with either matrix temperature or saturation. Differences in fracture saturation are noteworthy because of the importance of liquid flow into emplacement drifts and the potential for this flow to occur in fractures. All simulations, however, demonstrated some level of similarity in the evolution of fracture flow. All demonstrated dryout around the heaters, which started as segmented dryout zones at 3 months and coalesced into one large dryout zone encompassing both the heated drift and the wing heaters after 1 year of heating. Another similarity in all simulations was that increased fracture saturation first appeared beneath the wing heaters within 3 months of the onset on heating. In most simulations, elevated saturation was exhibited below the wing heaters approximately to the depth of the Tptpmn/Tptpll contact (i.e., 6 m below the wing heaters) within 3 months after the onset of heating (e.g., see Figure 18a). The zone of increased fracture saturation penetrated beyond the Tptpmn/Tptpll interface when either matrix permeability or the active fracture model γ was increased, or when either thermal conductivity or the van Genuchten α was decreased (e.g., see Figure 18b).

Essentially all simulations exhibited a zone of elevated fracture saturation above and at the sides of the boiling isotherm and the dryout zones. This high saturation zone was apparent in all simulations within 1 year after heating started, although the degree to which saturation and drainage increased below the test horizon varied significantly. Most simulations demonstrated a prominent thin layer of increased saturation immediately above the dryout zone and a less prominent layer of increased saturation immediately below the dryout zone. The zone of increased saturation below the dryout zone was most prominent at 3 months of heating and less prominent at 4 years of heating, although the zone of increased fracture saturation was expanded and better defined at 4 years compared with 1 year of heating (Figure 19). In addition, although the layer of increased saturation below the dryout zone was less defined than the layer above, the lower layer transitioned into a broad, extensive zone of increased saturation that continued downward for some distance. Both the upper and lower zones of increased fracture saturation are of potential interest because they could lead to increased flow of water into the drift from above and increased solute transport from the drift through fractures below.

The ability to replicate the observed temperatures is more easily evaluated using graphical comparisons of simulated and measured temperature in Boreholes 158 (vertically up), 160 (horizontal), and 162 (vertically down) located in a vertical plane 23 m from the thermal bulkhead. Simulated matrix and fracture temperatures are the same for all models except when the area modifier A_{mod} was less than 1.0; therefore, temperatures presented in the following graphs are representative of both the matrix and fracture continua. In general, the simulations were more successful in matching temperatures away from the heated drift than near it. The simulations consistently overpredicted temperatures near the drift wall. Neither variation of material and hydraulic properties nor the selection of the dual continuum conceptual model resulted in a significant decrease of temperature in this area. Plots of temperature at the three boreholes are compared with simulated temperatures for the basecase in Figure 20.

Relatively low temperatures observed near the heated drift were interpreted to be due to unmonitored heat and mass loss through the thermal bulkhead at the end of the heated drift. Loss of heat through the thermal bulkhead was estimated to be 6 kW by conduction and radiation and 22 kW by convection (Wagner, 1999). Wagner noted that the high level of uncertainty in these estimates was caused by the difficulty in making reasonable measurements. Heat loss through the bulkhead was probably not constant at 28 kW and, in fact, could have been quite variable, particularly in view of the complex effects of ventilation modifications in the connecting drift and barometric pumping (Chestnut, et al., 1998). Therefore, a constant pressure boundary condition was assigned to the drift wall in these simulations in the absence of actual boundary conditions measurements for the Drift-Scale Heater Test. This boundary condition allowed for the removal of sensible heat from the drift wall, presumably to account for the loss of enthalpy caused by water vapor loss through the bulkhead. This boundary condition, however, did not account for heat loss caused by conduction and radiation. If heat loss by conduction and radiation did, in fact, sum to 6 kW, then the percentage of heat reduction would be 11 percent when the canister heat load was 53 kW and 14 percent by the end of the test when the heat load was approximately 44 kW.

A 30-percent reduction in the canister heat load, which equated to a 15.9-kW reduction from the initial heat load and a 13.3-kW reduction at the end of the test, decreased, but did not eliminate, the discrepancy between measured and simulated temperatures after 4 years of heating (Figure 21). Examination of all nine temperature profiles in Figure 21, indicates that most main features in the thermal evolution measured at the three boreholes were captured in the simulations. The subtle heat pipes observed below the drift in Borehole 162 and beyond the end of the wing heaters have been reasonably, although not exactly, replicated in the simulation with a 30-percent reduction in the drift wall heat load (Figure 21). A heat pipe is still simulated above the drift in this case, even though no heat pipe was observed during the test.

The 30-percent reduction in heat load applied to the drift wall reduced temperatures near the drift to values closer to those measured, however, discrepancies between measured and simulated temperatures persist near the drift. Heat and mass transfer near the heated drift must either be different from that captured by the physics of the simulation, a mechanism for heat removal from the drift during the experiment must not be incorporated in the model, or heat loss by conduction and radiation must have exceeded the levels estimated by Wagner (CRWMS M&O, 1999).

A second discrepancy between observed and simulated temperatures was that a heat pipe was simulated above and, to a lesser degree, below the heated drift after 4 years of heating. The heat pipes

were not evident in the observed temperatures. No model modification attempted in these analyses eliminated evidence of the heat pipe, although reduction of fracture permeability did minimize the effect (Figure 22).

Temperatures calculated using a two-dimensional model were compared with similar results using a three-dimensional model to evaluate the effect of dimensionality. The comparison was made for the vertical plane located at the midpoint in the heated drift. The difference in temperatures calculated at the end of the 4-year heating phase is illustrated in Figure 23. The two-dimensional model calculated temperatures a maximum of 10.5 ºC higher at the boiling isotherm located above the outer wing heater. Also calculated was a slight decrease in temperature in the halo formed just within the boiling isotherm. The slightly lower temperatures calculated in the two-dimensional model are interpreted to be a consequence of increased condensed water caused by the slightly higher temperatures outside the boiling isotherm.

The effect of open versus closed drift-wall boundary conditions on calculated temperature was evaluated. Temperatures calculated for a model with the drift wall boundary treated as a Neumann boundary with no fluid and heat flow were compared with results from a model with a Dirichlet boundary condition at the drift wall. Temperature and saturation were allowed to vary while pressure was kept constant at one atmosphere at this boundary. The open boundary condition simulations resulted in reduced saturation at the drift wall. This lower saturation lowered the saturation-dependent thermal conductivity near the drift wall, resulting in higher temperatures in this region. As a consequence, temperatures calculated by the model with an open boundary at the drift wall were as much as 30 ºC higher near the drift and 20 ºC lower at the outer edge of the boiling isotherm (Figure 24). The open boundary at the drift wall is considered to more closely approximate the effects of heat and mass loss through the thermal bulkhead.

6. CONCLUSION

Numerical models were used to simulate thermal-mechanical and thermal-hydrological coupled processes in the fractured rock at the Drift-Scale Heater Test. The approach used to simulate thermal-mechanical coupled processes was to first determine the effects of temperature on deformation of the rock, then determine the change in permeability in response to the deformation. With this understanding, only the effects of mechanically induced fracture deformation on the rock-mass permeability were considered and a single continuum model was used to represent fracture permeability. The thermal-mechanical analyses were conducted in two dimensions based on a single continuum model using the FLAC code (Itasca Consulting Group, Inc., 2000).

Model results on thermally induced deformation around the heated drift and the mechanically induced rock permeability variations at specified thermal times and locations were compared with the corresponding measurements. Temperatures kriged at 1-m intervals were used as the basis for thermal load in the thermal-mechanical analyses. Analyses were predicated on either the Mohr-Coulomb or the ubiquitous fracture failure criterion. Simulations were performed to investigate the effects of rock-mass mechanical and strength properties, thermal expansion coefficients, and failure criteria on displacements and permeability during heating.

Regardless of the rock-mass properties, failure criterion, or treatment of the thermal expansion coefficient used in the simulations, the maximum principal stresses were in the rock mass at the crown and floor of the heated drift. The intermediate principal stress zones and the minimum principal stresses coincided with wing heater locations where the temperatures were greatest. The magnitude of thermally induced maximum and minimum principal stresses was found to be larger for cases using material and strength properties associated with higher rock-mass quality designations. This finding was expected because Young's modulus for a higher rock-mass quality category designation was larger than that of a relatively lower rock-mass quality category designation. The magnitudes of principal stresses were smaller for cases with the ubiquitous fracture failure criterion than for cases using the Mohr-Coulomb failure criterion.

Displacements estimated at specific anchors in four multiple-position extensometers were usually small when compared with measurements. All cases estimated an extension in the rock mass between two neighboring anchors of a multiple-position extensometer after 3 to 9 months of heating. This finding was not entirely supported by the measurements, which indicated compression of rock mass between anchors in several of the multiple-position extensometers. Furthermore, the measurements exhibited signs of local fracture slip. This phenomenon could not be modeled using the continuum approach.

A continuum model representing a deformation-permeability relationship was developed to assess thermal-mechanical effects on rock permeability. Modeling results indicated a reduction in permeability in the region that included the heated drift and the wing heaters. The largest reduction for subvertical fractures was associated with the rock mass located around the top and bottom of the heated drift, while, for subhorizontal fractures, the largest reduction was observed at the wing heaters.

The continuum analyses reasonably modeled permeability responses to the heating process, however, some obvious discrepancies between simulated and the measured permeabilities were identified. For example, the measured permeability at some locations indicated a consistent permeability reduction during heating, whereas simulated permeability enhancement at the beginning of heating was followed by a decrease. Furthermore, measured permeability exhibited recovery at some locations starting during the middle of the heating process, following a large reduction of permeability. One possible cause for this phenomenon was a reduction in fracture normal stress that resulted in a reduction in fracture closure, which, in turn, increased the fracture aperture. The other possibility was related to dilation induced by fracture shear displacement. None of the observed permeability recovery behavior was exhibited in the modeling results.

Thermal-hydrological analyses were performed with a three-dimensional numerical model using the multiphase simulator MULTIFLO (Painter, et al., 2001). A variably sized grid in the xz-plane, commonly referred to as an unstructured grid, was used to construct the numerical model. This allowed for higher resolution near the heated drift and the wing heaters, areas with the greatest gradients in temperature and saturation. The xz-plane was extruded as 14 planes in the y-direction to give the model its third dimension. The medium was represented as a dual continuum, one for the matrix and one for the fractures. Three conceptualizations were used to implement matrix-fracture interactions. The effects of different conceptual models on calculated temperature and saturation were compared. Conceptual models for the Drift-Scale Heater Test were mostly evaluated by comparing fracture saturation simulated by different models and by comparing simulated and measured temperatures.

The basecase consisted of infiltration at 3.0 mm/yr, the active fracture model (Liu, et al., 1998) with $\gamma = 0.41$. Based on replication of temperatures measured at three boreholes (158, 160, and 162) located at the midpoint of the heated drift, the best match between measured and simulated temperature was given by the basecase simulation with the active fracture model conceptualization (Liu, et al., 1998) and with the canister heat load reduced by 30 percent. Simulated temperatures from this conceptualization captured most, but not all, salient features in the measured temperatures. In particular, simulated temperatures closest to the drift did not reflect the transient features exhibited in the measured temperatures. Additionally, a heat pipe simulated above the drift wall (Borehole 158) at 4 years of heating was not seen in the measured data. Reduction, but not elimination, of the heat pipe could be achieved by decreasing the fracture permeability of the simulation that included the 30-percent reduction in drift-wall heat load.

Fracture saturation simulations indicated that zones of increased saturation form below the outer wing heaters by 3 months of heating. By 1 year of heating, these zones increased in size and were found both above and below the wing heaters. By this time, a prominent dryout zone had developed which encompassed the combined heated drift-wing heater region. In addition, a prominent zone of increased fracture saturation had formed beneath the full footprint of the field-scale experiment at 1 year of heating.

The dryout zone thickness in the fracture continuum approached 13 m in height at the end of the 4-year heating phase. The zone of greatest fracture saturation was slightly diminished in extent at this time, appearing mostly near the ends of the wing heaters, although the thickness of these increased saturation zones increased. These results suggest that increased saturation would be available for fracture flow near the edges of the boiling isotherm and the dryout zones. This tendency could become important if the increased fracture saturation led to focused seepage into emplacement drifts, possibly resulting in an environment that enhanced corrosion by causing increased relative humidity and liquid saturation.

The effect of dimensionality (i.e., two-dimensional versus three-dimensional) on temperature was evaluated. A maximum reduction in temperature of about 10 ºC near the wing heaters was calculated after 4 years of heating when a three-dimensional model was used compared with a two-dimensional model. Changing the drift wall from a closed boundary to an open boundary increased temperatures near the drift by a maximum of 30 ºC and decreased temperatures at the outer extent of the boiling isotherm by about 20 ºC. Higher temperatures at the drift wall are attributed to lower thermal conductivities caused by drier rock.

7. ACKNOWLEDGMENTS

This paper was prepared to document work performed by the Center of Nuclear Waste Regulatory Analyses (CNWRA) for the Nuclear Regulatory Commission (NRC) under Contract No. NRC-02-02-012. The activities reported here were performed on behalf of the NRC Office of Nuclear Material Safety and Safeguards, Division of High-Level Waste Repository Safety. This paper is an independent product of the CNWRA and does not necessarily reflect the view or regulatory position of the NRC. The NRC staff views expressed herein are preliminary and do not constitute a final judgment or determination of the matters addressed or of the acceptability of a license application for a geologic repository at Yucca Mountain.

REFERENCES

Bandis, S.C., A.C. Lumsden, and N.R. Barton. "Fundamentals of Rock Joint Deformation." *International Journal of Rock Mechanics and Mining Sciences & Geomechanics Abstracts*. Vol. 20, No. 6. pp. 249–368. 1983

Barton, N.R. and S.C. Bandis. "Effects of Block Size on the Shear Behavior of Jointed Rock." *23rd U.S. Symposium on Rock Mechanics*. Berkeley, California: The University of California at Berkeley. 1982.

Barton, N.R., S.C. Bandis, and K. Bakhtar. "Strength, Deformation, and Conductivity Coupling of Rock Joints." *International Journal of Rock Mechanics and Mining Sciences & Geomechanics Abstracts*. Vol. 22, No. 3. pp. 121–140. 1985.

Brooks, R.H. and A.T. Corey. "Properties of Porous Media Affecting Fluid Flow." *Journal of Irrigation and Drainage Engineering*. Vol. 92. pp. 61–88. 1966.

Chestnut, D.A., M.J. Peters, T.A. Buscheck, and R.N. Datta. "Relative Humidity Response to Barometric Pressure Change in an Underground Heated Drift at Yucca Mountain." *Geological Society of America Abstract with Programs—1998 Annual Meeting*. Boulder, Colorado: Geological Society of America. p. A–362. 1998.

CRWMS M&O. "Multiscale Thermohydrologic Model." ANL–EBS–MD–000049. Rev. 00 ICN 02. Las Vegas, Nevada: CRWMS M&O. 2001.

CRWMS M&O. "Ground Control for Emplacement Drifts for SR." ANL–EBS–GE–000002. Rev. 00. Las Vegas, Nevada: CRWMS M&O. 2000.

CRWMS M&O. "TBV-332/TBD-325 Resolution Analysis: Geotechnical Rock Properties." B00000000–01717–5705–00134. Rev. 00. Las Vegas, Nevada: CRWMS M&O. 1999.

CRWMS M&O. "Ambient Characterization of the Drift-Scale Test Block." BADD00000–01717–5705–00001. Rev. 01. Las Vegas, Nevada: CRWMS M&O. 1997a.

CRWMS M&O. "Drift Scale Test Design and Forecast Results." BAB000000–01717–4600–00007. Rev. 01. Las Vegas, Nevada: CRWMS M&O. 1997b.

CRWMS M&O "Yucca Mountain Site Geotechnical Report." B00000000–01717–5705–00043. Vol. 1. Rev. 01. Las Vegas, Nevada: CRWMS M&O. 1997c.

Elsworth, D. "Thermal Permeability Enhancement of Blocky Rocks: One-Dimensional Flow." *International Journal of Rock Mechanics and Mining Sciences & Geomechanics Abstracts*. Vol. 26, No. 3/4. pp. 329–339. 1989.

Elsworth, D. and C.R. Mase. "Chapter 8: Groundwater in Rock Engineering." *Comprehensive Rock Engineering* 1. J.A. Hudson, ed. New York City, New York: Pergamon Press. pp. 201–226. 1993.

Hsiung, S.M., D.D. Kana, M.P. Ahola, A.H. Chowdhury, and A. Ghosh. NUREG/CR–6178, "Laboratory Characterization of Rock Joints." Washington, DC: NRC. 1994.

Itasca Consulting Group, Inc. "FLAC—Fast Lagrangian Analysis of Continua." Version 4.0. Minneapolis, Minnesota: Itasca Consulting Group, Inc., 2000.

Lichtner, P.C. and M.S. Seth. "Multiphase-Multicomponent Nonisothermal Reactive Transport in Partially Saturated Porous Media." *Proceedings of the International Conference on Deep Geological Disposal of Radioactive Waste, Winnipeg, Manitoba, Canada, September 16–19, 1996.* Toronto, Ontario, Canada: Canadian Nuclear Society. pp. 133–142, 1996.

Liu, H.H., C. Doughty, and G.S. Bodvarsson. "An Active Fracture Model for Unsaturated Flow and Transport in Fractured Rock." *Water Resources Research* Vol. 34, No. 10. pp. 2,633–2,646. 1998.

Mualem, Y. "A New Model for Predicting Hydraulic Conductivity of Unsaturated Porous Media." *Water Resources Research*. Vol. 12. pp. 513–522, 1976.

Ofoegbu, G.I. "Thermal-Mechanical Effects on Long-Term Hydrological Properties at the Proposed Yucca Mountain Nuclear Waste Repository." CNWRA 2000-03. San Antonio, Texas: CNWRA. 2000.

Painter, S.L, P.C. Lichtner, and M.S. Seth. "MULTIFLO User's Manual, MULTIFLO Version 1.5–Two-Phase Nonisothermal Coupled Thermal-Hydrologic-Chemical Flow Simulator." Revision 3. Change 0. San Antonio, Texas: CNWRA. 2001.

Schrauf, T.W. and D.D. Evans. "Laboratory Studies of Gas Flow Through a Single Natural Fracture." *Water Resources Research*. Vol. 22, No. 7. pp. 1,038–1,050. 1986.

Snow, D.T. "Rock Fracture Spacings, Openings, and Porosities." *Journal of the Soil Mechanics and Foundations Division*. Vol. 94, No. SM1. pp. 73S91. 1968.

TRW Environmental Safety Systems, Inc. "Thermal Tests, Thermal-Hydrological Analyses/Model Report." Las Vegas, Nevada: TRW Environmental Safety Systems, Inc. 2000.

van Genuchten, M.Th. "A Closed-Form Equation for Predicting the Hydraulic Conductivity of Unsaturated Soils." *Soil Science Society of American Journal*. Vol. 44. pp. 892–898. 1980.

Wagner, R.A. "Assessment of heat loss through the Drift-Scale Heater Test Bulkhead." Memorandum (October 21) to M.T. Peters. Las Vegas, Nevada: CRWMS M&O. 1999.

Witherspoon, P.A., J.S.Y. Wang, K. Iwai, and J.E. Gale. "Validity of Cubic Law for Fluid Flow in a Deformation Rock Fracture." *Water Resources Research*. Vol. 16, No. 6. pp. 1,016–1,024. 1980.

List of Figures

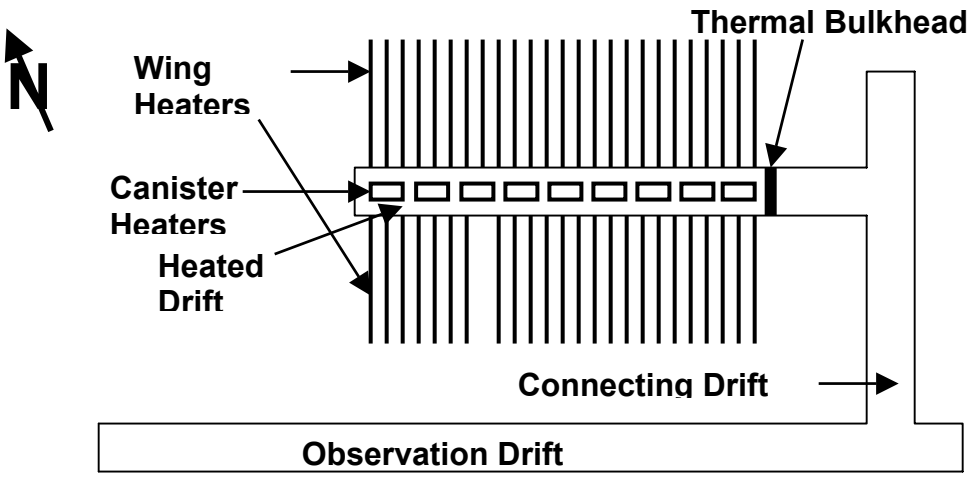

Figure 1. Plan-view Schematic of the Drift-Scale Heater Test

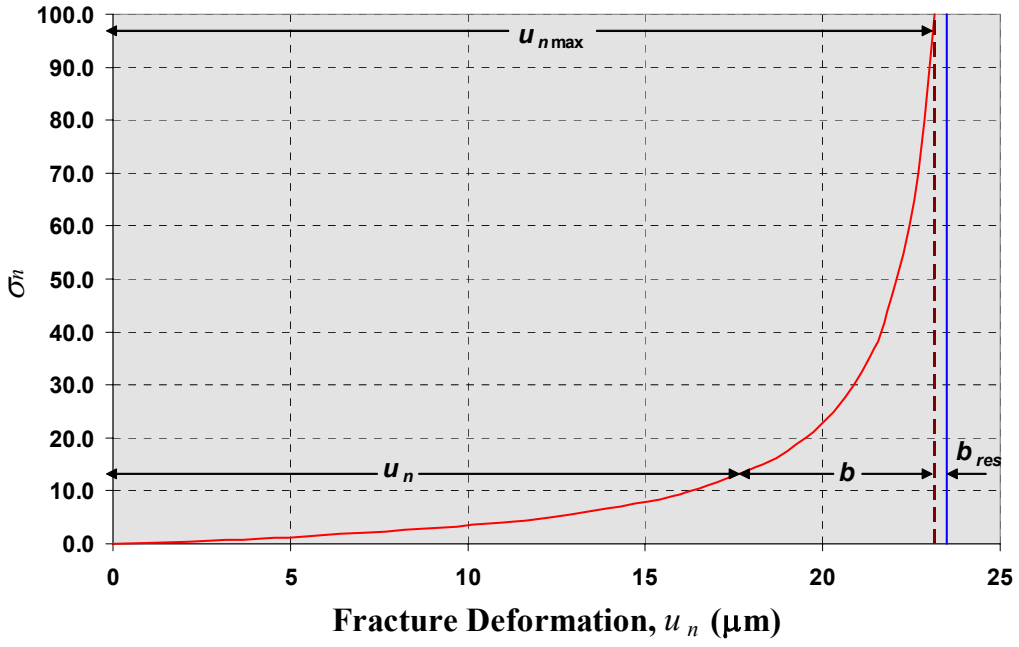

Figure 2. Fracture Normal Stress and Deformation Curve

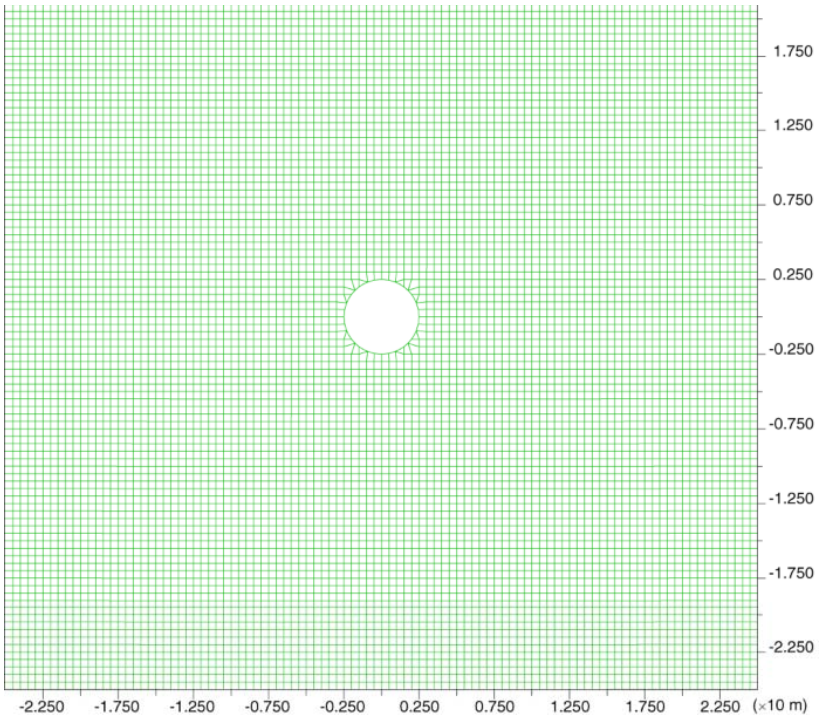

Figure 3. Closeup of the Two-Dimensional Grid Assigned to Thermal-Mechanical Model

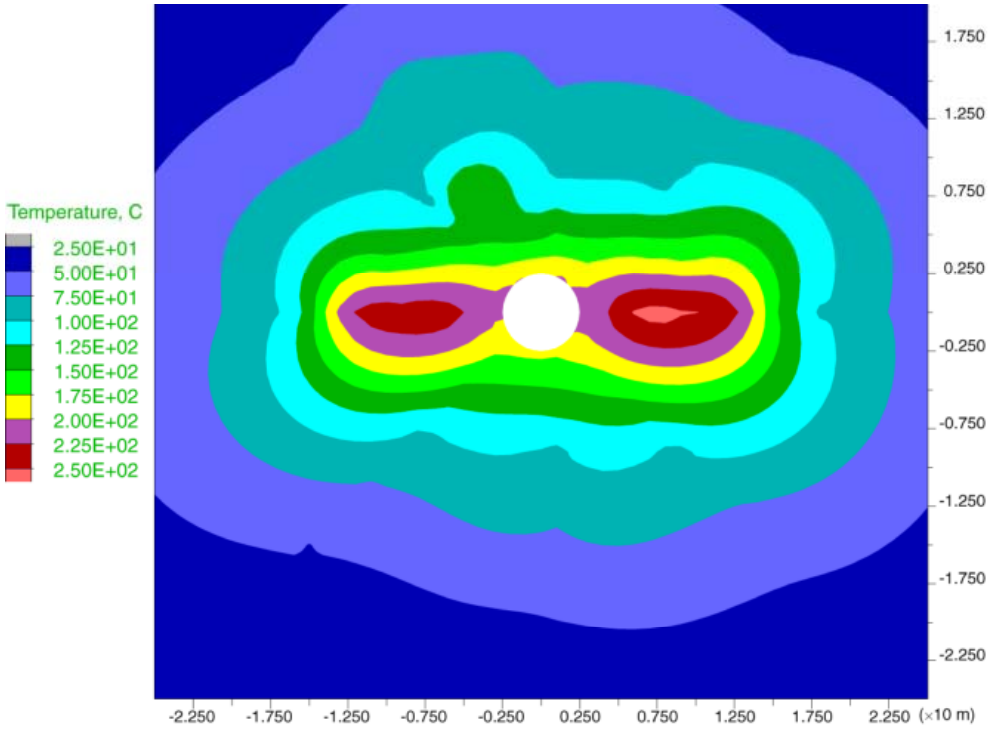

Figure 4. Measured Temperature (ºC), 23 m From the Thermal Bulkhead After 4 Years of Heating

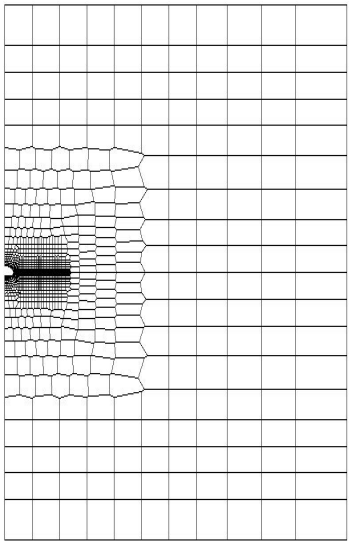

Figure 5. Unstructured Grid Assigned to the Thermal-Hydrological Model

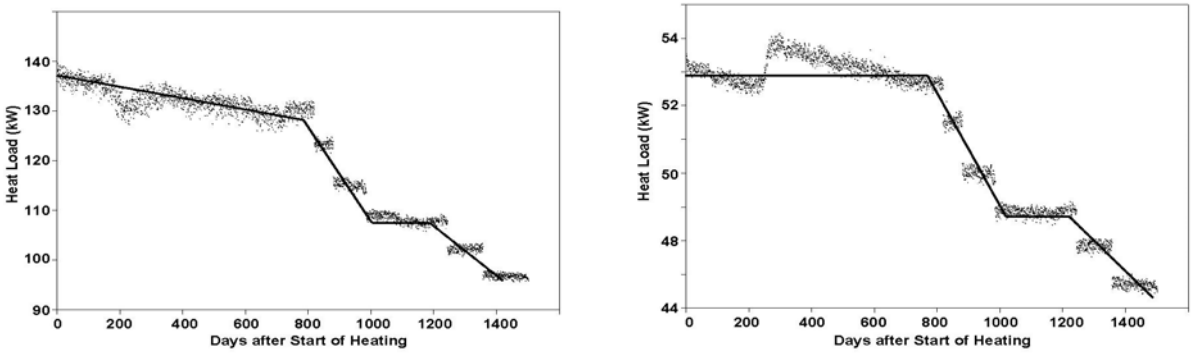

Figure 6. Measured (Dots) and Simulated (Lines) Heat Load for the Wing (Top) and Canister (Bottom) Heat Sources

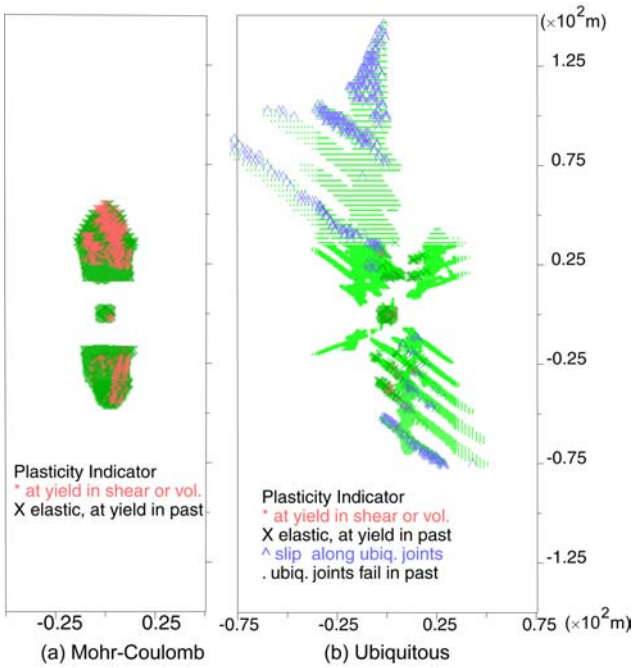

Figure 7. Thermally Induced Rock-Mass Yielding at 4 Years

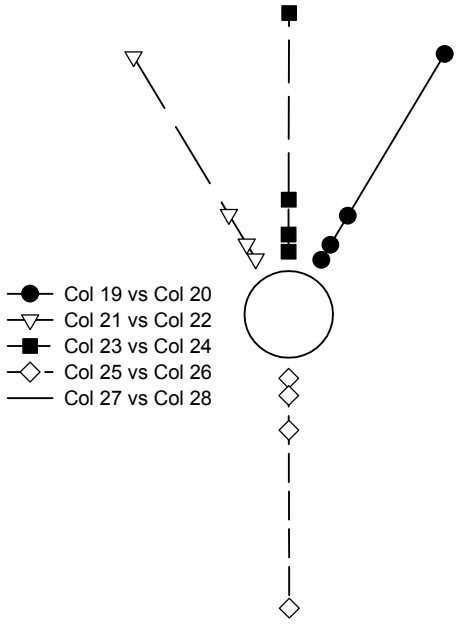

Figure 8. Relative Positions of Multiple-Position Extensometer Anchors with Respect to Drift

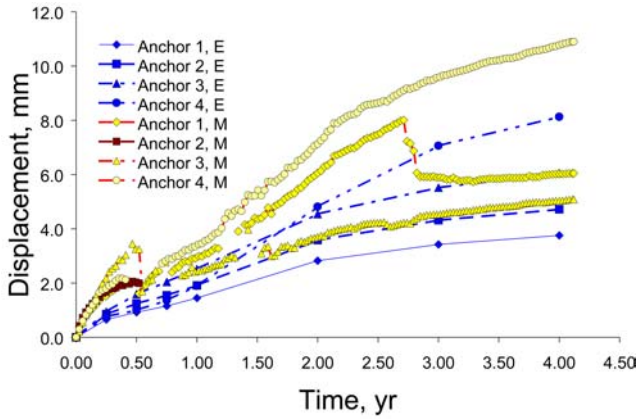

Figure 9. Measured and Simulated Anchor Displacements for MPBX7

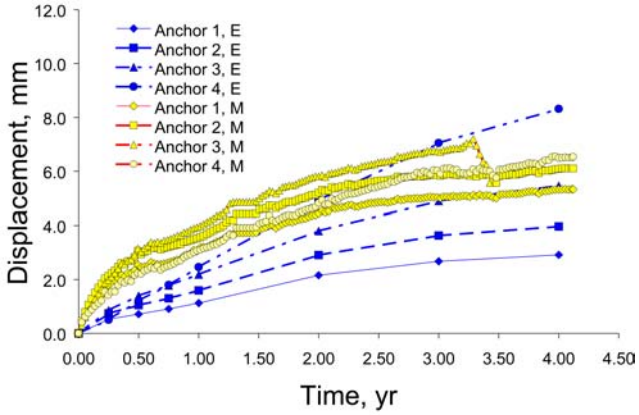

Figure 10. Measured and Simulated Anchor Displacements for MPBX8

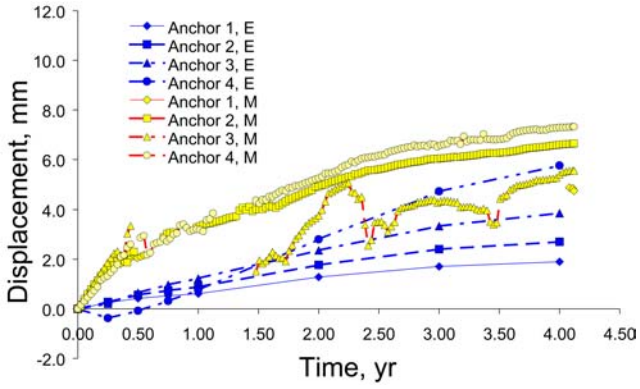

Figure 11. Measured and Simulated Anchor Displacements for MPBX9

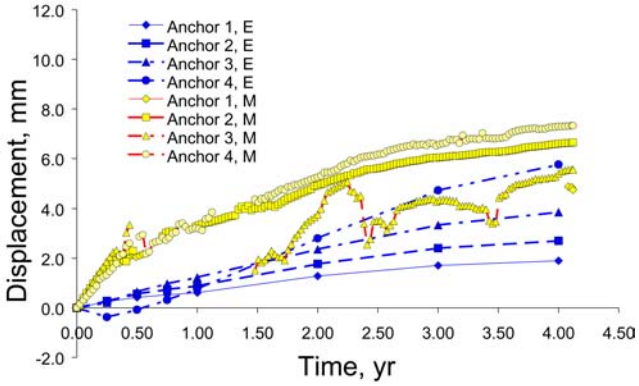

Figure 12. Measured and Simulated Anchor Displacements for MPBX10

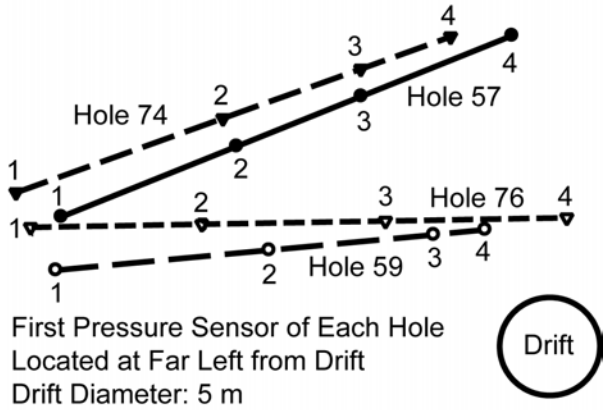

Figure 13. Location of Hydrologic Boreholes

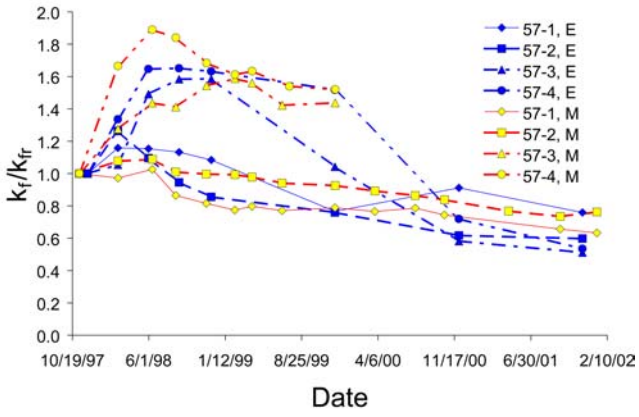

Figure 14. Measured and Simulated Permeability Variations for Borehole 57

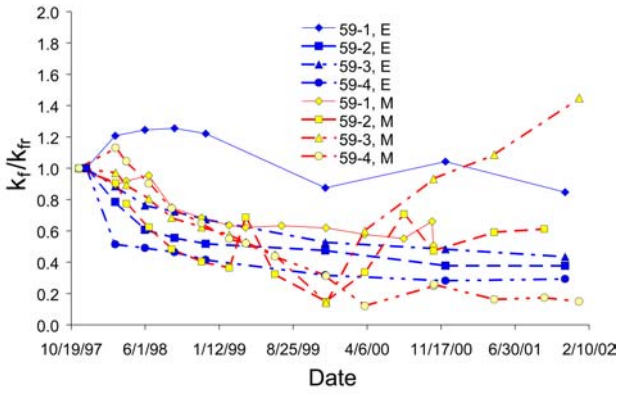

Figure 15. Measured and Simulated Permeability Variations for Borehole 59

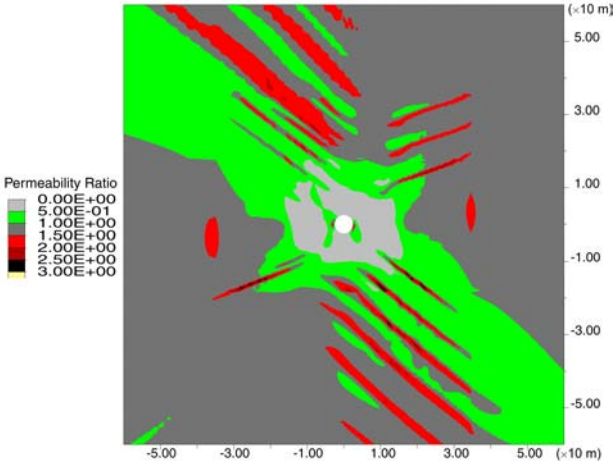

Figure 16. Simulated Permeability Contour Plot for a Model Using the Ubiquitous Failure Criterion

(a)

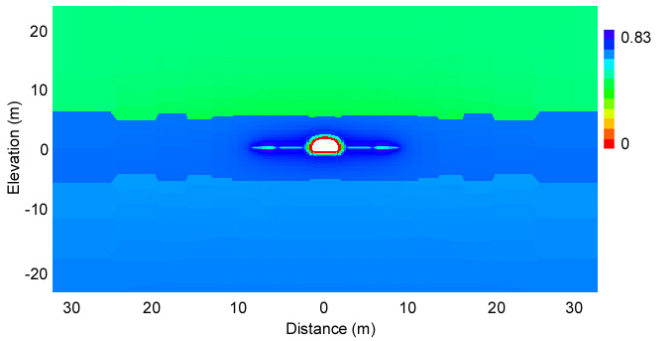

(b)

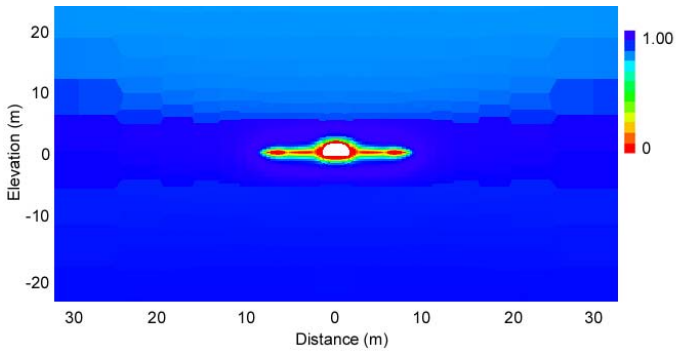

(c)

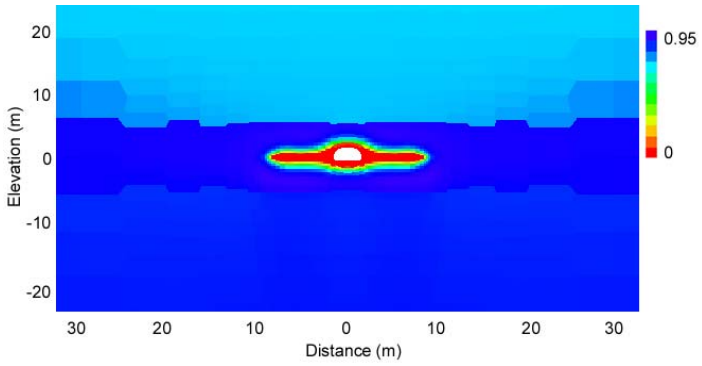

Figure 17. Simulated Matrix Saturation at 1 Year Illustrating (a) Small , (b) Moderate, and (c) Large Dryout Zone Development

(a)

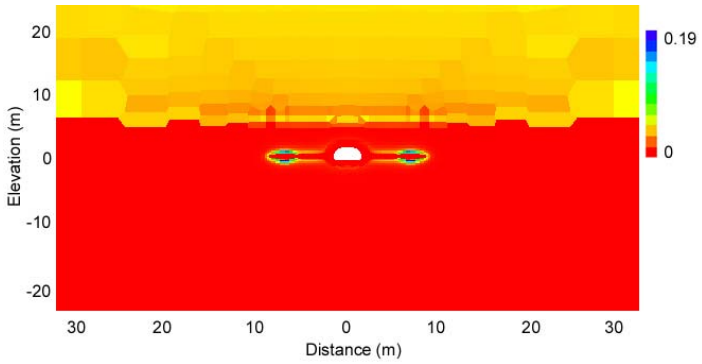

(b)

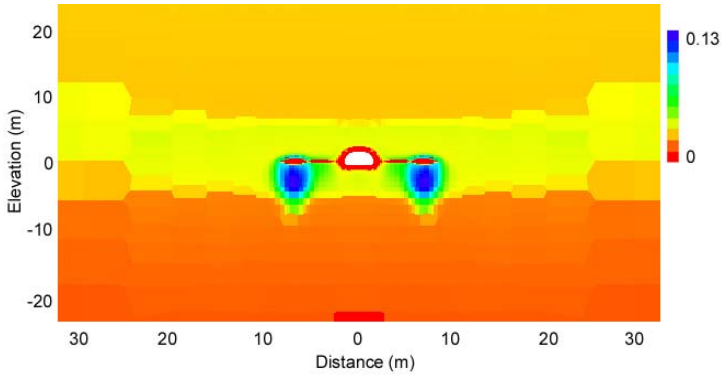

Figure 18. Simulated Fracture Saturation at 3 Months Illustrating (a) Moderate and (b) Large Increased Fracture Saturation Zone Development Below the Wing Heaters

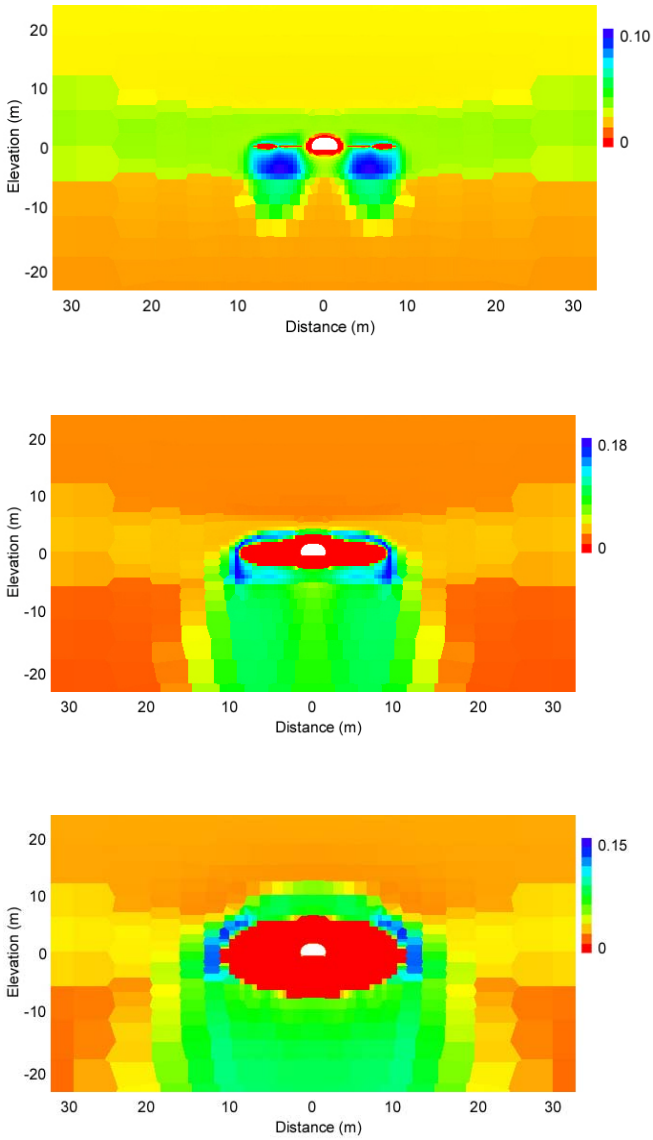

Figure 19. Fracture Saturation After 3 Months, 1 Year, and 4 Years of Heating for Typical Simulation

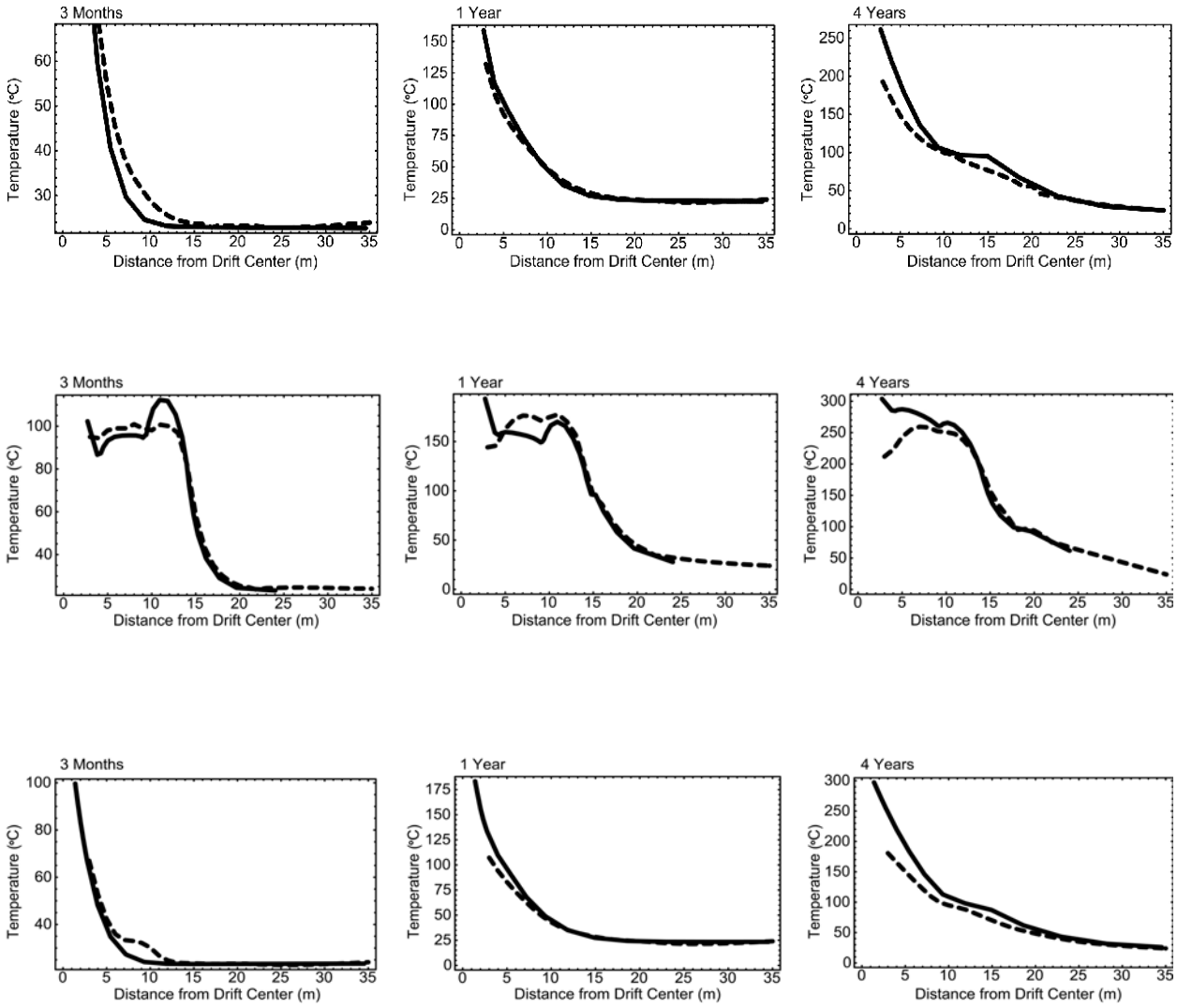

Figure 20. Comparison of Measured Temperature Versus Simulated Matrix Temperature at 3 Months (Left), 1 Year (Center), and 4 Years (Right) for Boreholes 158 (Top), 160 (Middle), and 162 (Bottom) for the Basecase

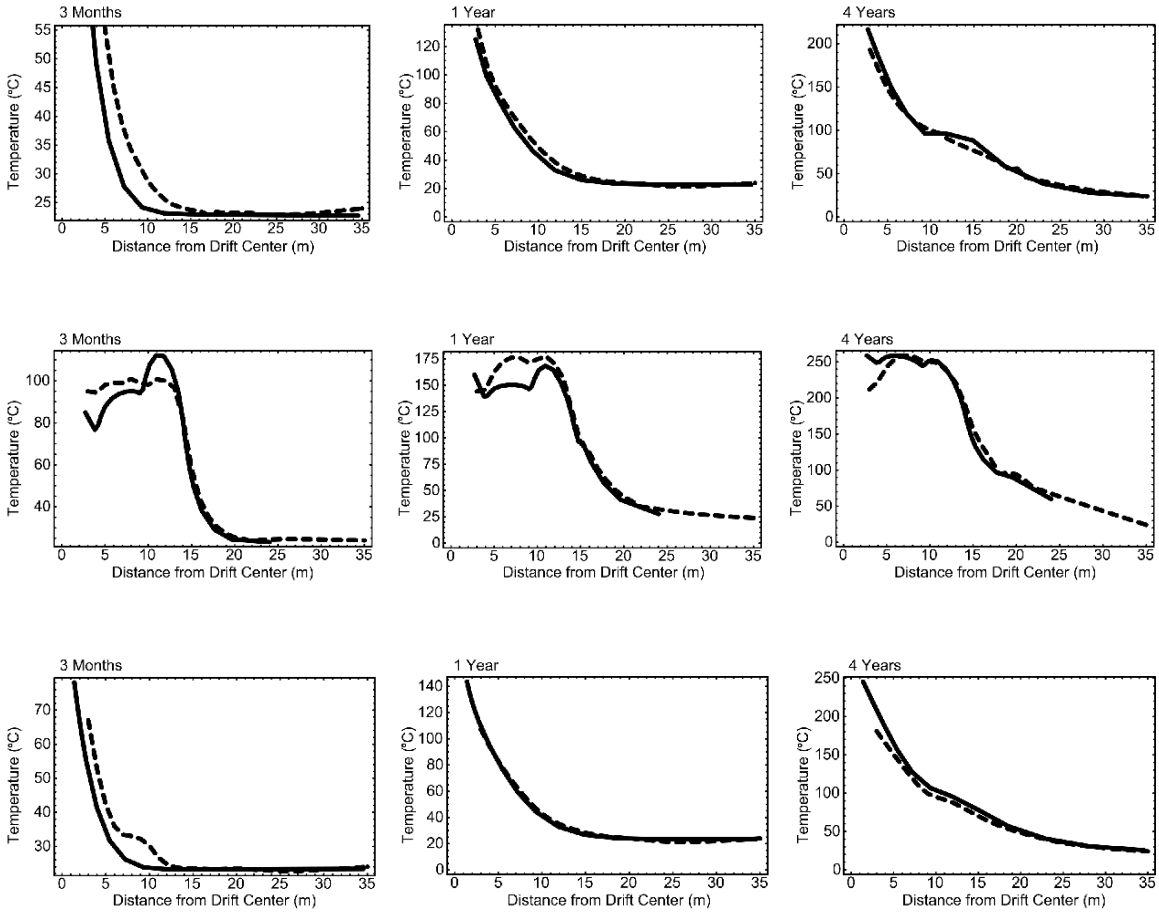

Figure 21. Comparison of Measured Temperature Versus Simulated Matrix Temperature at 3 Months (Left), 1 Year (Center), and 4 Years (Right) for Boreholes 158 (Top), 160 (Middle), and 162 (Bottom) with Drift-Wall Heat Load Decreased by 30 Percent

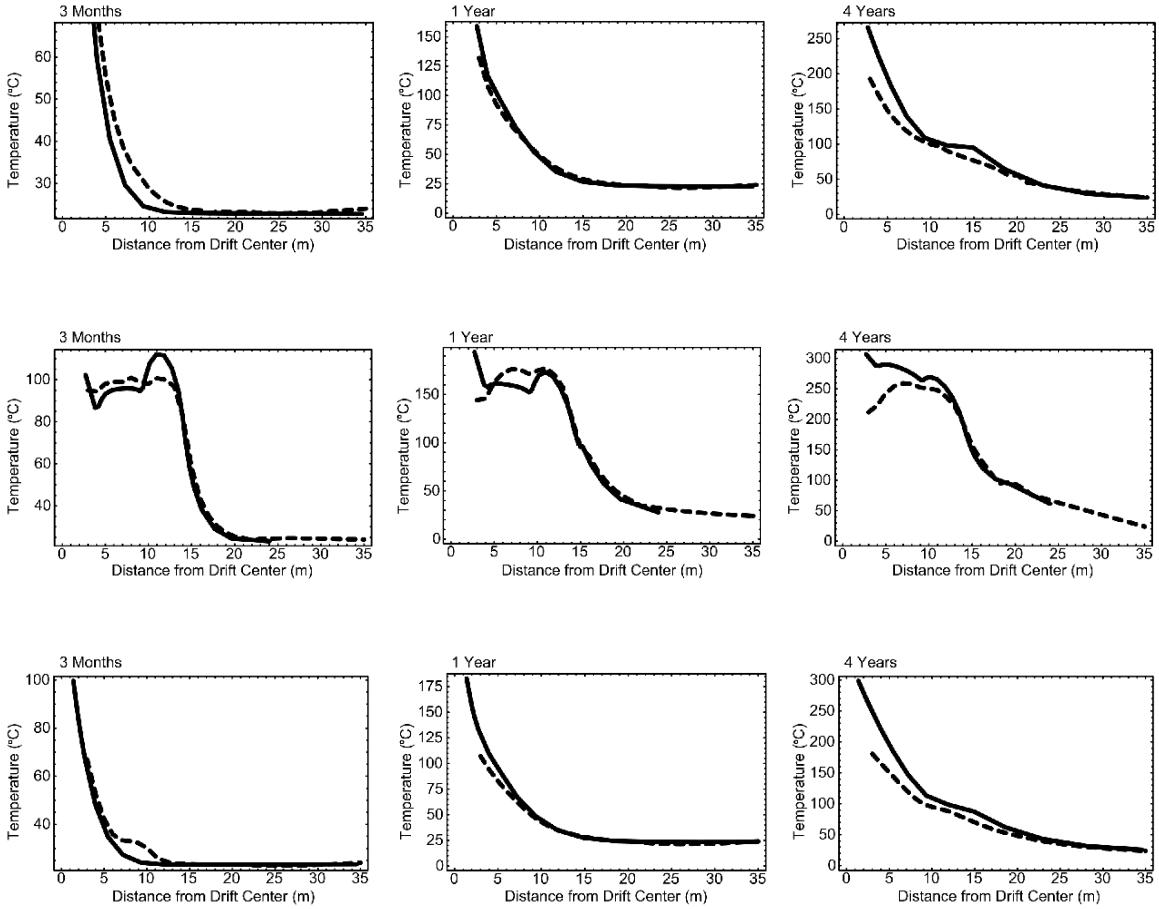

Figure 22. Comparison of Measured Temperature Versus Simulated Matrix Temperature at 3 Months (Left), 1 Year (Center), and 4 Years (Right) for Boreholes 158 (Top), 160 (Middle), and 162 (Bottom) with Fracture Permeability Decreased by 10 Times

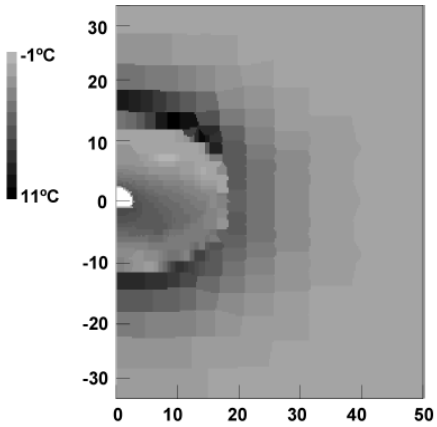

Figure 23. Temperature Difference Between Two-Dimensional and Three-Dimensional Models After 4 Years of Heating

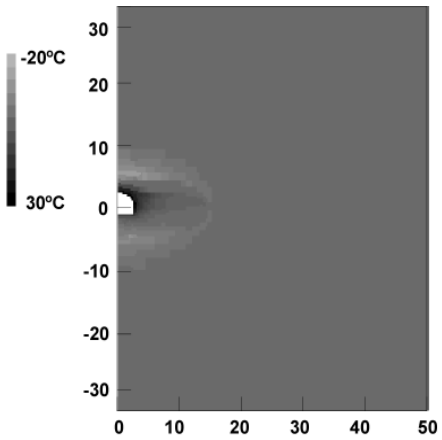

Figure 24. Temperature Difference Between Open and Closed Boundary at the Drift Wall